

Numerical Study on Post-Earthquake Fire Resistance of Concrete Filled Tube Column

Gandhi Krutika Naresh

A Dissertation Submitted to
Indian Institute of Technology Hyderabad
In Partial Fulfillment of the Requirements for
The Degree of Master of Technology



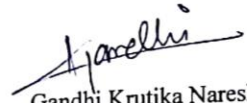
भारतीय प्रौद्योगिकी संस्थान हैदराबाद
Indian Institute of Technology Hyderabad

Department of Civil Engineering

July 2018

Declaration

I declare that this written submission represents my ideas in my own words, and where others' ideas or words have been included, I have adequately cited and referenced the original sources. I also declare that I have adhered to all principles of academic honesty and integrity and have not misrepresented or fabricated or falsified any idea/data/fact/source in my submission. I understand that any violation of the above will be a cause for disciplinary action by the Institute and can also evoke penal action from the sources that have thus not been properly cited, or from whom proper permission has not been taken when needed.


Gandhi Krutika Naresh

CE16MTECH11018

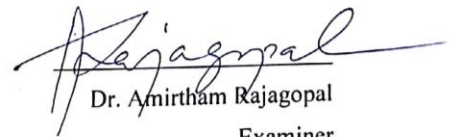
Approval Sheet

This thesis entitled **Numerical Study on Post-Earthquake Fire Resistance of Concrete Filled Tube Column** by **Gandhi Krutika Naresh** is approved for the degree of Master of Technology.



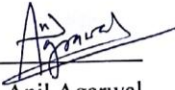
Dr. Gangadharan R

Examiner
Dept. of Mechanical Engg.
IITH



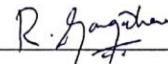
Dr. Amirtham Rajagopal

Examiner
Dept. of Civil Engg.
IITH



Dr. Anil Agarwal

Adviser
Dept. of Civil Engg.
IITH



Dr. Gangadharan R

Chairman
Dept. of Mechanical Engg.
IITH

Acknowledgements

I would like to express my heartfelt gratitude to my advisor **Dr. Anil Agarwal** for the continuous support of my M. Tech study and related research, for his patience, motivation, and immense knowledge. His guidance, timely advice and assistance during the project helped me in all the time of study and writing of this thesis.

I am also thankful to Mr. Hemanth Kumar Chinthapalli and other lab-mates for their valuable assistance and support during the project. I am also indebted of my classmates and friends for their help and support throughout M. Tech. tenure.

I would like to pay high regards to my parents for their sincere encouragement and inspiration.

Above all, I thank almighty for the successful completion of this thesis work.

Gandhi Krutika Naresh

Abstract

Earthquakes cause devastating damage to the buildings and structures, but if earthquake events are followed by fire may cause more damage than the earthquake itself. After a major earthquake, the ability of the structure to resist fire drastically reduces. So, the risk of fires following earthquakes are considered significantly higher than normal.

Recently, steel-concrete composite structures have been increasingly used in modern structures due to the respective advantages of steel and concrete. Concrete filled steel tube (CFT) columns are an excellent example of composite construction because of its efficiencies and advantages. One important advantage is their high fire resistance because in this system, the steel tube prevents the concrete core from spalling and the concrete core provides additional capacity to the steel tube. Many researchers have studied behavior of axially loaded CFT columns under cyclic loading and fire loading separately.

In present study, the finite element model built and validated with the previously conducted experiments on CFT columns under seismic loading and studied the reduction in strength due to it. Also, the behavior of axially loaded circular CFT columns exposed to fire is modelled using the finite element analysis package ABAQUS. A three step sequentially coupled nonlinear thermal-stress analysis is conducted for a series of columns available from the literature. The developed model is validated with experimental results by comparing fire resistance in simulations results and experimental tests.

The aim of study was to study the post-earthquake fire behavior of concrete filled tube columns, for the same numerical study is conducted to examine behavior of pre-damaged CFT columns exposed to fire after being subjected to cyclic loads. Different level of damage was induced in the columns to study the effect of residual drifts and damage on fire resisting capacity and compared the same with undamaged CFT columns. Total five columns with varying was simulated for post-earthquake fire behavior. Damage was initially induced by subjecting them to different level peak displacement. Later, the simulated model for undamaged and damaged CFT columns were subjected to nodal time-temperature data calculated by the heat analysis following the ASTM E119 fire curve, to examine the effect. Residual deformation due to cyclic loading and applied axial load showed substantial effect on fire resisting capacity of the columns.

Table of Contents

| | |
|---|----|
| List of Figures | 7 |
| List of Tables | 8 |
| 1. Introduction | 9 |
| 2. Literature Review | 10 |
| 3. Objective and Scope..... | 12 |
| 4. Finite Element Model for simulation of CFT columns subjected to cyclic loading | 13 |
| 4.1. Element Model | 13 |
| 4.2. Material Model..... | 14 |
| 4.3. Steel-Concrete Interface..... | 16 |
| 5. Validation of the FEM Model for CFT columns under Fire loading..... | 17 |
| 5.1. CFT columns details taken for validation. | 17 |
| 5.2. Verification of thermal analysis..... | 18 |
| 5.3. Comparison between numerical and experimental results | 20 |
| 6. Validation of the FEM Model for CFT columns under Cyclic loading..... | 25 |
| 6.1. CFT columns details taken for validation under cyclic loading. | 25 |
| 6.2. Procedure of simulation for cyclic loading | 28 |
| 6.3. Validation Results | 29 |
| 7. Finite element simulation of Post-Earthquake Fire scenario for CFT column | 35 |
| 7.1. Details of specimens under study | 35 |
| 7.2. Element and Material model..... | 35 |
| 7.3. Step-wise procedure for analysis | 36 |
| 8. Results and discussions. | 38 |
| 9. References..... | 45 |
| Annexure..... | 47 |
| 1. Horizontal load versus horizontal displacement hysteretic curves (Xilin Lu et al.) | 47 |
| 2. Nonlinear isotropic/kinematic hardening model..... | 48 |
| 3. Material Properties | 49 |

List of Figures

| | |
|--|----|
| Figure 1 San-Francisco Post Earthquake fire (source -USGS)..... | 10 |
| Figure 2 The Great Kanto Earthquake - Fire event (Source Great Kantō Earthquake.com) | 11 |
| Figure 3- a -Meshed Solid Element- Concrete model b – Meshed Shell element Steel model | 13 |
| Figure 4- Effect of different plastic hardening models of steel material | 14 |
| Figure 5- Damage plasticity behavior (a) compression and (b) tension for concrete | 16 |
| Figure 6-Comparison of experimental and simulation time versus temperature curve for C-02 . | 18 |
| Figure 7Comparison of experimental and simulation time versus temperature curve for C-17... | 19 |
| Figure 8Comparison of experimental and simulation time versus temperature curve for C-25... | 19 |
| Figure 9 Comparison of Temperature-Time curves using different thermal property models..... | 20 |
| Figure 10- Deformed shape after exposure to standard fire, for column C-05..... | 21 |
| Figure 11-Deformed shape after exposure to standard fire, for column C-17..... | 21 |
| Figure 12 Comparison of axial displacement versus fire exposure time for experiment and predicted by simulation..... | 21 |
| Figure 13-Comparison of error with calculated and measured failure time with relative slenderness ratio | 23 |
| Figure 14-Comparison of different end conditions of column | 24 |
| Figure 15-Comparison of different initial geometric imperfection on slender column..... | 24 |
| Figure 16- Test Setup (Xilin Lu et al.)..... | 26 |
| Figure 17-Displacement history as per experiment | 27 |
| Figure 18-Failure of specimen- R3M7 | 27 |
| Figure 19- Representation of FEM model | 28 |
| Figure 20- Comparison of simulated lateral force versus displacement curve with experiments | 30 |
| Figure 21-Horizontal load versus horizontal displacement- hysteretic curves for simulated columns | 32 |
| Figure 22- Comparison of validated results with experimental results | 32 |
| Figure 23- Displacement history according to ATC- 24 recommendation..... | 37 |
| Figure 24-Scheme of analysis | 38 |
| Figure 25- C-05 Axial displacement vs time of exposure for different damage level..... | 39 |
| Figure 26 SQ-01- Axial displacement vs time of exposure for different damage level | 40 |
| Figure 27 C-26- Axial displacement vs time of exposure for different damage levels | 41 |

| | |
|--|----|
| Figure 28 SQ-20 Axial displacement vs time of exposure for different damage levels | 42 |
| Figure 29 SQ-24 Axial displacement vs time of exposure for different damage levels | 43 |

List of Tables

| | |
|---|----|
| Table 1-List of table validated from literature for CFT under Fire | 17 |
| Table 2-Results for validation columns from literature- Predicted and measured failure time.... | 22 |
| Table 3- Test data of column specimens (Xilin Lu et al.) | 25 |
| Table 4- Result Summary of experiments (Xilin Lu et al.) | 28 |
| Table 5- Results from validation of CFT columns under cyclic loading..... | 30 |
| Table 6-Details of CFT columns under the study of post-earthquake fire scenario | 35 |

1. Introduction

Earthquakes cause devastating damage to the buildings and structures, but if earthquake events are followed by fire may cause more damage than the earthquake itself. After a major earthquake, the ability of the structure to resist fire drastically reduces. So, the risk of fires following earthquakes are considered significantly higher than normal. Our modern buildings codes give design values to have adequate resistance against an expected level earthquake, and considers sufficient fire safety, but codes give design criteria considering these events to occur separately. However, fire following an earthquake event is not uncommon. Earthquake shaking causes movement or damage of equipment and containers. This shaking can result in contact with ignition sources, such as open flames or electrical open wires. We cannot prevent earthquakes or predict accurately, only damage caused by it can be minimized by proper design of structure and planning. Sometimes many structures withstand earthquake shakings but they may have experienced non-structural damage which increases the likelihood of fire and impairs the functionality of the building.

Post-earthquake fire poses a serious threat to structural stability detrimental to the life safety of the occupants and saving lives and properties. Therefore, it is necessary to consider post-earthquake fire condition in the design of a building constructed in a seismic zone, especially for the post-disaster facilities. Steel structures are particularly vulnerable to fire hazard.

Recently, steel-concrete composite structures have been increasingly used in modern structures due to the respective advantages of steel and concrete i.e. their high strength and ductility, structural efficiency, cost benefits and construction economy. Steel-concrete composite construction is also beneficial from a fire resistance perspective. Steel structures utilizing composite columns can potentially achieve high fire resistance due to the presence of concrete (owing to its lower thermal conductivity and expansion coefficients), which has good fire resistance characteristics. So, concrete filled steel tube (CFT) columns are an excellent example of composite construction because of its efficiencies and advantages.

The mechanical strength of steel reduces drastically at high temperature. Outer steel tube starts buckling locally in the early stage of fire losing its strength to sustain the load. On the other hand, the concrete core and steel tube gets damaged if structure subjected to shakes before the fire.

Although the fire following earthquake has a devastating effect, much of attention has not been given by researchers. There is a need to investigate resistance capacity of structures under the combined effect of earthquake and fire.

2. Literature Review

On April 18, 1906, an earthquake and subsequent fires devastated San Francisco, California, leaving more than 3,000 people dead and destroying more than 28,000 buildings. The greatest devastation resulted from the fires that quickly followed the quake. The initial tremors destroyed the city's water mains, leaving firefighters with no means of combating the growing blaze, which burned for several days and consumed much of the city Figure 1.

Similarly, in 1923, Tokyo earthquake -Great Kanto Earthquake Figure 2, of magnitude 7.9, burning 38.3 sq. km. and reaching firestorm proportions, with a tragic death toll of about 140,000. Most of the deaths and damage are attributed to fires fueled by flimsy wooden houses and fanned by high winds in Yokohama and Tokyo City. The quake destroyed the city's water mains, paralyzing the fire department. A 300-foot-tall "fire tornado" blazed across the area of Sumida River where tens of thousands people were gathered, out of 44,000 people only 300 could survive. [1]



Figure 1 San-Francisco Post Earthquake fire (source -USGS)



Figure 2 The Great Kanto Earthquake - Fire event (Source Great Kantō Earthquake.com)

Number of researchers studied the effect of Post-Earthquake Fire on the behavior of structures. Yassin et al. (2010) conducted an analytical study on the performance of moment resisting steel frame in Post-Earthquake Fire. And they found that performance of the structure highly depends upon the residual lateral deformations present in structure caused by the earthquake. As fire induces deformation asymmetrically due to degradation of material properties and gets add-up to previously present residual deformations in structure causing early failure. While the frames with no residue displacement from a prior seismic loading given the relatively long time of failure.

Xilin Lu et al experimentally investigated the seismic behavior of 12 CFRT column specimens subjected to reversed cyclic loading and constant axial load. They also performed the nonlinear full range analysis of these composite columns for simulating the test results and to do the parametric study. The effects of varying width-thickness ratio of the steel plate, axial compression ratio, and different strengths of infilled concrete on the seismic behavior of CFRT columns were studied and shows that thicker steel tube increases the strength, higher concrete strength results in higher ultimate strength but larger strength degradation and lower energy dissipation compared to columns with normal strength concrete.

Reza Imani et al. performed experimental studies for understanding the behavior concrete filled double- skin tube (CFDST) columns under post-earthquake fire conditions. They tested three

columns of the same dimension with different damage condition. Out of three, one column was tested in undamaged condition subjected to fire to know the fire resistance of column under axial load and fire. The other two columns were first subjected to cyclic lateral loading by subjecting lateral drifts to incorporate moderate and high levels of damage and later columns was tested for fire resistance. Both of the specimens were pushed to the maximum drift of 6-6.5% with a different level of residual drifts of 1.4% and 3.9% for moderate and high levels, respectively. All columns were subjected to standard ASTM E119 time-temperature curve with constant axial load until columns fail. Overall results show there is very less difference in fire resisting capacity for all three columns, shows that CFDST columns perform very well under the post-earthquake fire scenario. Along with experiments, they also conducted FEM analysis by using ABAQUS and LS-DYNA to simulate the behavior of CFDST columns under post-earthquake fire scenario. Analytical results showed sufficient match with experiments.

3. Objective and Scope

Post-earthquake fire can lead to a rapid collapse of structures which are partially damaged by the earthquake event. As there are almost no established post-earthquake fire provisions by codes and standards, the investigations are therefore needed for the buildings or structures. The principal aim of this research is to study the behavior of CFT columns subjected to post-earthquake fire scenario. For this, the finite element model is created using ABAQUS for simulating cyclic loading test on CFT column and its validation with available experimental data. Also, the FE model was created to study the effect of fire loading on axially loaded CFT columns. Finally, combined seismic-thermal FE-model was built to study the effect of different level of earthquake damage in CFT column and the fire resistance capacity of previously damaged columns.

4. Finite Element Model for simulation of CFT columns subjected to cyclic loading

4.1. Element Model

Stress-Displacement elements are needed to capture the non-linear cyclic behavior of concrete. The 3D solid element is the best choice to model the concrete core as solid elements in ABAQUS and can capture large deformation and plastic strains. Because of the high computational time of 20 node element during analysis, 3-D 8 node solid elements with reduced integration are used to model concrete part in the present study. This element is referred to as C3D8R in ABAQUS element library. For modeling steel along with solid elements, shell elements are also a proper choice as the thickness of steel tube is significantly smaller than column dimension. Shell elements are usually used for modeling one-dimensional elements where one dimension is smaller than the other two. As the thickness of steel tube is smaller (5 mm or less), the problem can arise when solid elements are used for modeling thin-walled tube, like a few integration points along thickness or poor aspect ratio. Considering all aspects, S4R, 4-noded solid elements are used for steel tube modeling.

Also, Prior analytical studies on steel-concrete composite columns showed that 4-node shell (S4R) element for modeling steel and 8-node solid (C3D8R) element for concrete provides acceptable results if suitable mesh pattern is used. (Reza Imani et. al). So, steel tube was meshed uniformly using S4R element and the concrete core was meshed using C3D8R. The following Figure 3(a) and (b) shows meshed concrete and steel elements respectively

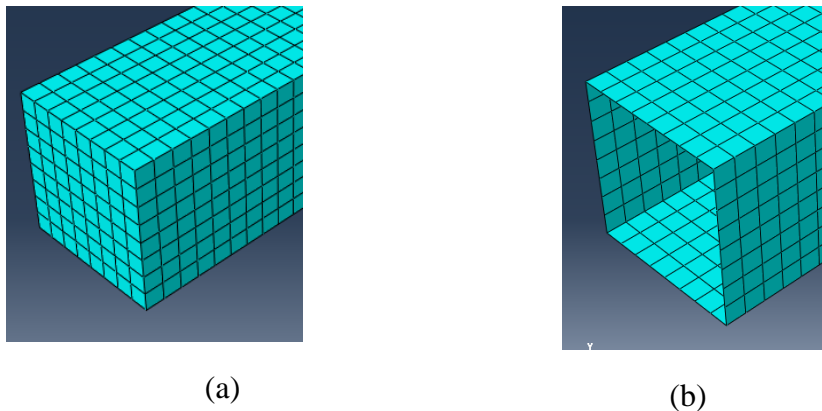


Figure 3- a -Meshed Solid Element- Concrete model b – Meshed Shell element Steel model

4.2. Material Model

Steel Material

A bilinear model is used for the steel material consisting of a linear elastic phase and post-yield linear hardening phase having 1% to 2% of initial stiffness. The classical metal plasticity model present in ABAQUS is used for modeling the plastic behavior of steel. It uses Von Mises yield surfaces with associated flow rule. Various hardening rules are considered (Isotropic, Kinematic linear and non-linear) for modeling steel material under cyclic loading.

When an elastic-perfectly plastic model with isotropic hardening is used, loading surface expands uniformly and cannot account for bauschinger effect. Isotropic hardening means that the yield surface changes size uniformly in all directions such that the yield stress increases (or decreases) in all stress directions as plastic straining occurs. So, Isotropic hardening models fail to give realistic results.

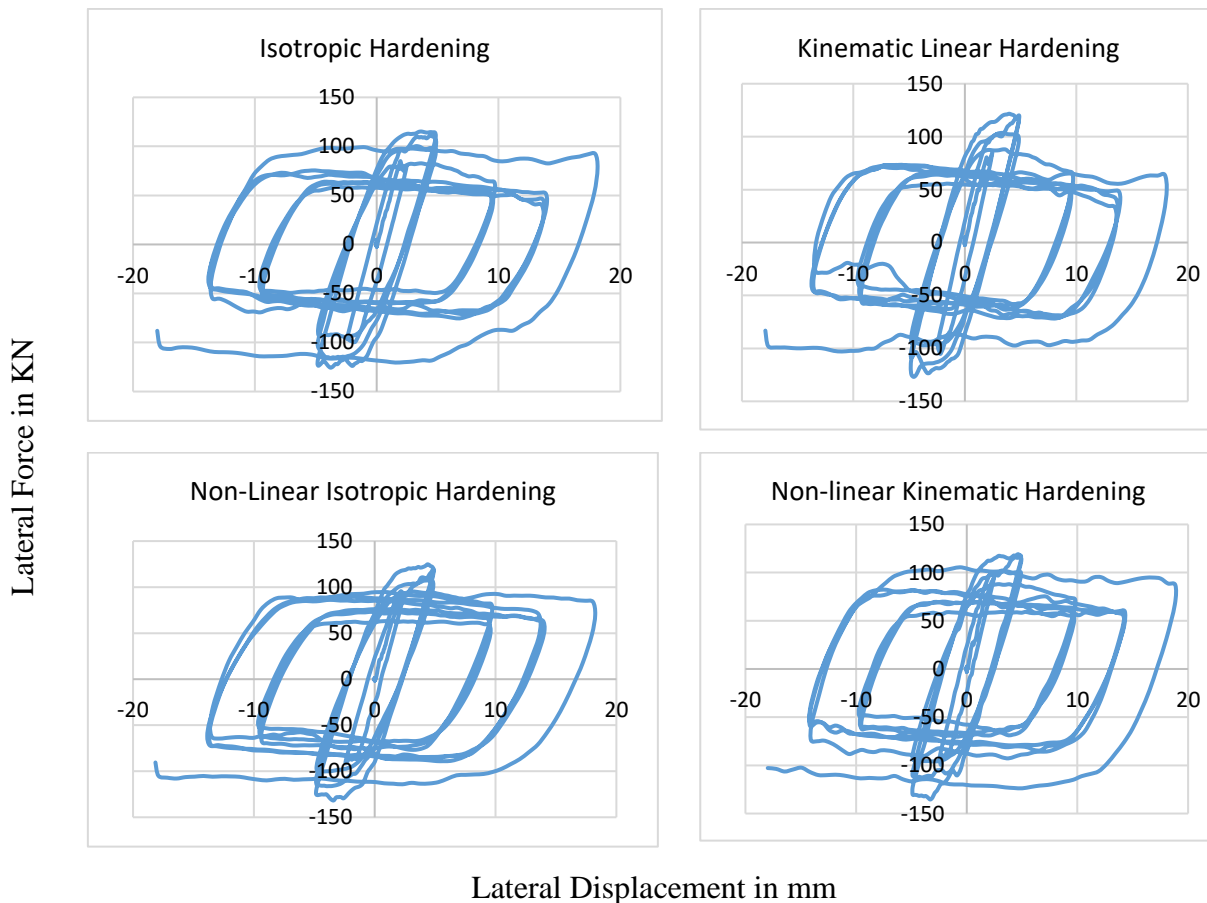


Figure 4- Effect of different plastic hardening models of steel material

Two kinematic hardening models are provided in ABAQUS to model the cyclic loading of metals. The linear kinematic model approximates the hardening behavior with a constant rate of hardening. The more general nonlinear combined isotropic-kinematic model will give better predictions but requires more detailed calibration of stress-strain curves according to test data. The linear kinematic hardening model is used for study and it uses Von Mises Yield surface. Due to unavailability of tensile test data for steel used in the experiment, parameters required for modeling nonlinear combined kinematic and isotropic model are taken from Dso. et al. for the study. A detailed explanation of parameter value is given in the Annexure.

The graph shown in Figure 4 are Lateral load (KN) versus lateral displacement (mm) for a different type of hardening models. From the above graphs, it can be seen that for the present study kinematic linear hardening model gives a proper representation of hysteretic curve for cyclic loading. Also steel plastic hardening model does not have much effect on the behavioral result.

Concrete Material

Concrete Core was modeled using Damage Plasticity model which is implemented in ABAQUS. It includes degradation of elastic stiffness in tension and compression upon unloading and also stiffness recovery of load reversal to consider the effect of closed cracks.

Figure 5 (a) and (b) shows Response of concrete to uniaxial loading in tension and compression respectively. When the concrete specimen is unloaded from any point on the strain softening branch of the stress-strain curves, the unloading response is weakened and the elastic stiffness of the material appears to be damaged (or degraded). The degradation of the elastic stiffness is characterized by two damage variables, d_t and d_c , which are assumed to be functions of the plastic strains, temperature. (ABAQUS theory Manual- SIMULIA 2012)

For uniaxial compression and tension, the stress-strain relation under uniaxial loading in the damage-plasticity behavior displayed in

Figure 5 can be written as:

$$\sigma_c = (1 - d_c) E_0 (\epsilon_c - \epsilon_c^{pl})$$

$$\sigma_t = (1 - d_t) E_0 (\epsilon_t - \epsilon_t^{pl})$$

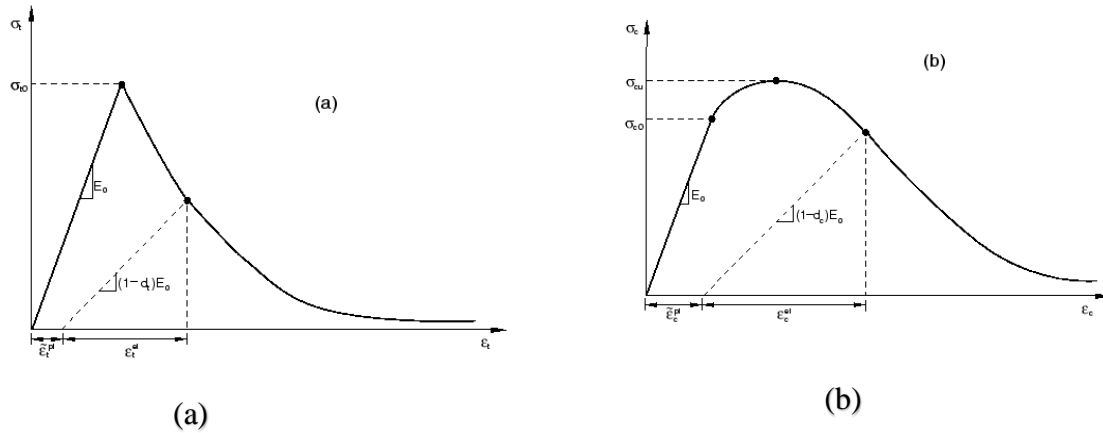


Figure 5- Damage plasticity behavior (a) compression and (b) tension for concrete

Sub-indexes c and t refers to compression and tension respectively.

For uniaxial cyclic loading-unloading conditions, the damage plasticity model assumes that the degradation in the elastic stiffness is given by

$$E = (1-d) E_0$$

4.3. Steel-Concrete Interface

Contact between steel and concrete is required to be modeled while the study of the concrete filled column to ensure that forces are transferred between steel tube and concrete core whenever required and both materials get separate from each other when needed. When the CFT column is axially loaded, forces are required transferred between steel and concrete while due to local deformation of tubes steel surface gets separate from the concrete core.

Steel- Concrete interface is modeled using the surface to surface contact interaction module present in ABAQUS. Hard contact property is used for contact in the normal direction, so that elements of steel and concrete in contact are able to transfer pressure or forces when comes in contact. While contact in the tangential direction is modeled with the friction of value equal to 0.2 to 0.6. This can be defined in ABAQUS under tangential property model of general contact by giving a penalty of required friction.

For studying the effect of the perfect bond between steel and concrete surface in the initial stage of loading, columns were analyzed again by tying steel inner surface with the concrete outer surface. In this concrete surface is used as master surface and inner steel surface as slave surface.

5. Validation of the FEM Model for CFT columns under Fire loading

The three-dimensional numerical model was validated by comparing the simulations with experimental fire resistance tests from NRCC report.

5.1. CFT columns details taken for validation.

Above analytical approach was used to predict the behavior of CFT columns under fire loading. The CFT columns included in this analytical study are shown in Table 1 along with their reported material and geometric material properties. All are circular CFT columns tested by NRCC researchers according to the ASTM E119 standard fire test. Lie, T. T.; Chabot, M. (1992) reported these results. Columns have sectional diameter ranging from 141.3 to 406.4 mm, steel tube wall thicknesses varying from 4.78 to 12.7mm and have constant length of 3810 mm. Only middle 3048mm length of column was exposed to fire. All columns have fixed boundary condition except column C-06 which has pinned-pinned condition. Relative slenderness of column is calculated as per of EN 1994-1-2. (given in Annex)

Table 1-List of table validated from literature for CFT under Fire

| Sr. No. | Column no. | Dia. of conc. Core (D) | Steel tube thickness (t) | Fc | Fyd | Relative slenderness ratio (λ) |
|---------|------------|------------------------|--------------------------|------|-----|--|
| 1 | C-02 | 141.3 | 6.55 | 33.1 | 350 | 0.55 |
| 2 | C-04 | 141.3 | 6.55 | 31 | 350 | 0.55 |
| 3 | C-05 | 168.3 | 4.78 | 32.7 | 350 | 0.50 |
| 4 | C-06 | 168.3 | 4.78 | 32.7 | 350 | 0.7 |
| 5 | C-08 | 168.3 | 4.78 | 35.5 | 350 | 0.50 |
| 6 | C-11 | 219.1 | 4.78 | 31 | 350 | 0.40 |
| 7 | C-13 | 219.1 | 4.78 | 32.3 | 350 | 0.40 |
| 8 | C-17 | 219.1 | 8.18 | 31.7 | 350 | 0.37 |
| 9 | C-22 | 273.1 | 5.56 | 27.2 | 350 | 0.32 |
| 10 | C-23 | 273.1 | 12.7 | 27.4 | 350 | 0.28 |
| 11 | C-25 | 323.9 | 6.35 | 27.6 | 350 | 0.27 |
| 12 | C-26 | 323.9 | 6.35 | 24.3 | 350 | 0.26 |
| 13 | C-28 | 355.6 | 6.35 | 23.8 | 350 | 0.24 |
| 14 | C-29 | 355.6 | 12.7 | 25.4 | 350 | 0.22 |
| 15 | C-30 | 406.4 | 12.7 | 27.6 | 350 | 0.20 |
| 16 | C-53 | 355.6 | 6.35 | 42.4 | 300 | 0.26 |
| 17 | C-57 | 406.4 | 6.35 | 44 | 300 | 0.23 |
| 18 | C-59 | 406.4 | 12.7 | 37.4 | 300 | 0.20 |
| 19 | C-60 | 406.4 | 12.7 | 45.1 | 300 | 0.20 |

5.2. Verification of thermal analysis

A first validation step consisted of comparing the evolution of temperature along the fire exposure time in the numerical simulations with the temperatures recorded in the tests at those sectional points where thermocouples were installed. The comparison between measured and calculated temperatures is shown in Figure 6 and Figure 7 for some of the column specimens studied.

However, some of the tests did not follow as closely as desired the standard fire curve, which have introduced some distortions in the fire response of the columns. The maximum difference in temperatures was up to 100 °C. Thus, the real furnace temperature-time curve reported from the fire tests was applied in the simulations to check the difference in response. Figure 8 shows comparison of axial displacement versus failure time for column C-25 with temperature loading through thermal analysis and temperature loading from temperature-time curve reported from the fire tests. It shows that difference in temperature does not affect the actual response of column.

Figure 9 shows comparison of temperature versus time curve by using different thermal properties i.e Eurocode thermal properties and Thermal properties using Lie Model, (mentioned in Annex) at different depth in column. Temperature using Eurocode thermal properties are slightly more than Lie's model.

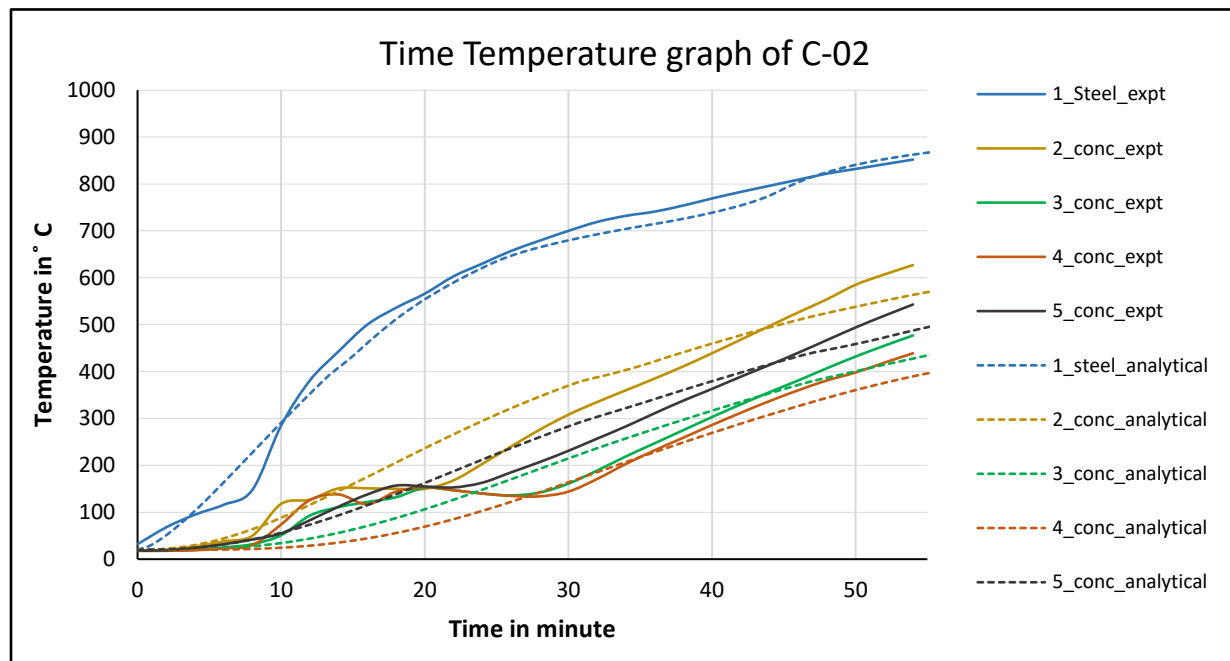


Figure 6-Comparison of experimental and simulation time versus temperature curve for C-02

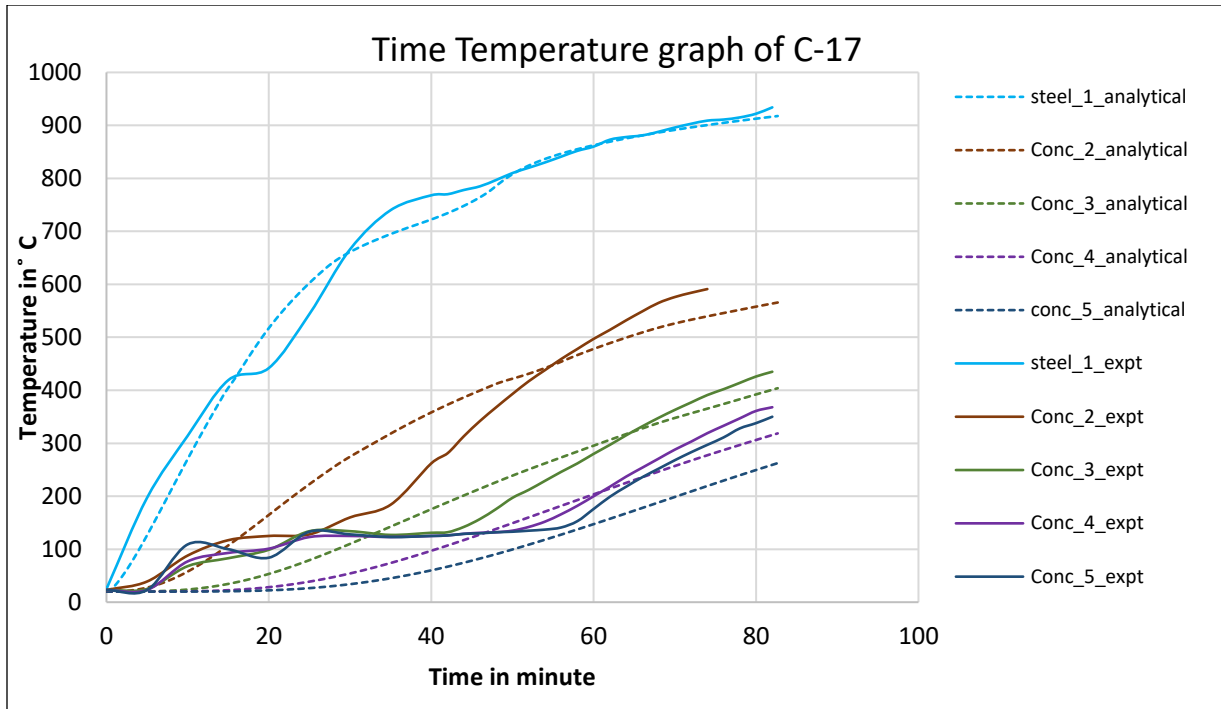


Figure 7 Comparison of experimental and simulation time versus temperature curve for C-17

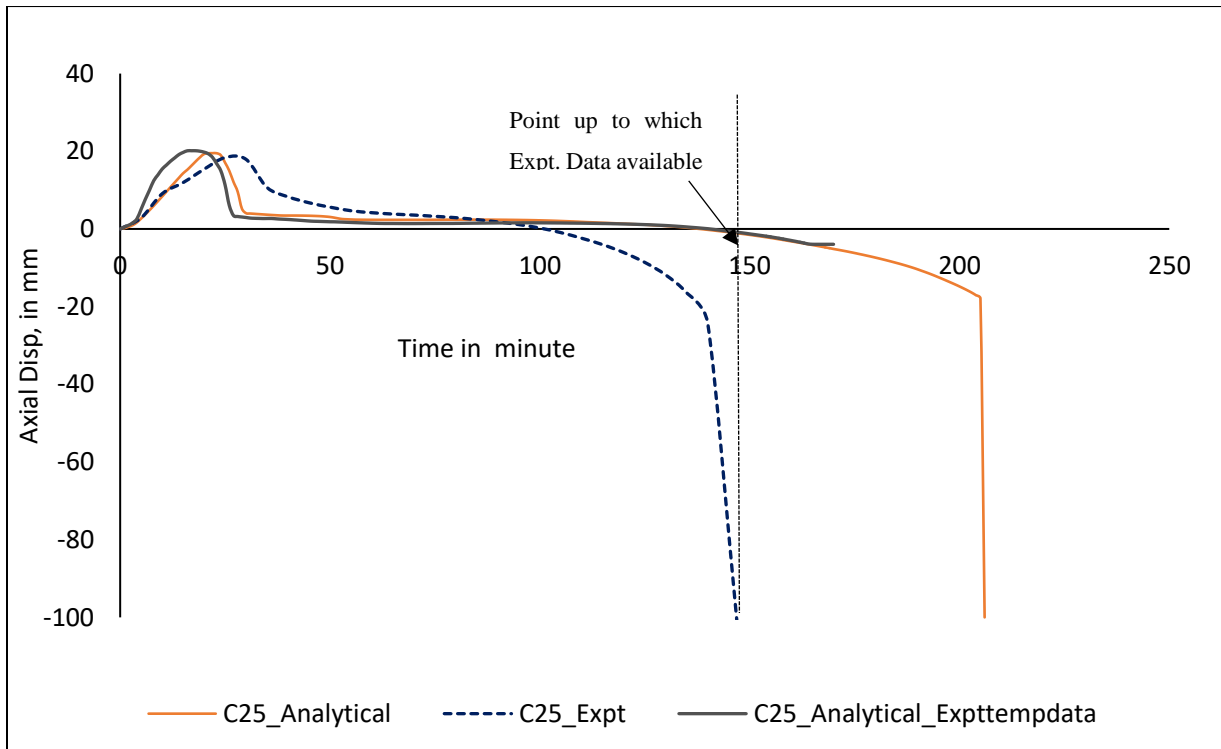


Figure 8 Comparison of experimental and simulation time versus temperature curve for C-25

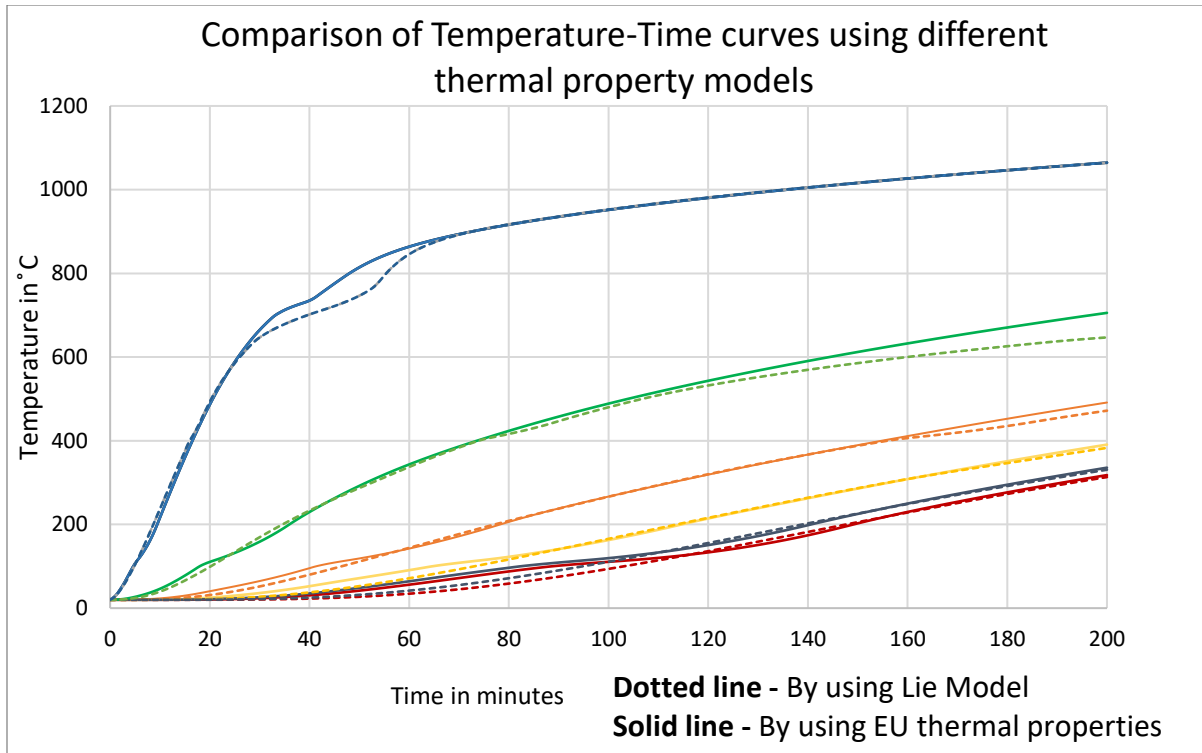


Figure 9 Comparison of Temperature-Time curves using different thermal property models

5.3. Comparison between numerical and experimental results

The axial displacement at the top of the column versus the fire exposure time was obtained for each of the column of the Table 1 and the curves are matched with the curves obtained in the fire resistance test. Figure 10 and Figure 11 shows the result of the numerical simulations of Column C-05 and column C17, where the axial displacement field along the column and its deformed shape after failure can be seen in part (a), together with the respective picture of the fire test and part (b) shows comparison of axial displacement versus fire exposure time for experiment and predicted by simulation for respective circular columns.

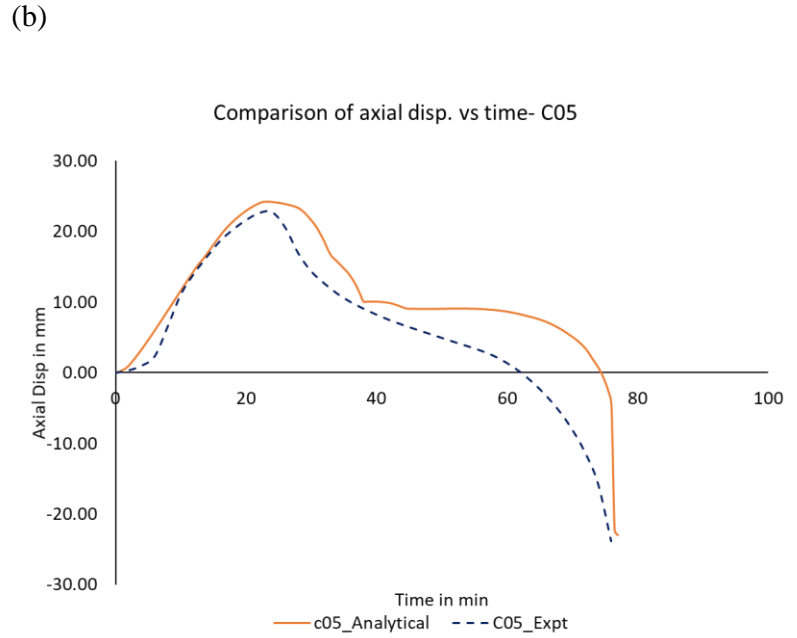
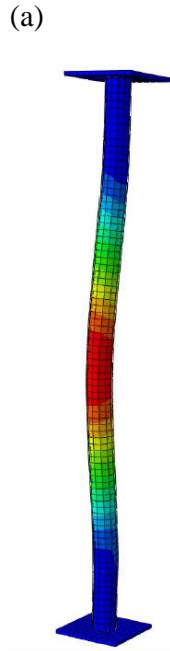


Figure 10- Deformed shape after exposure to standard fire, for column C-05

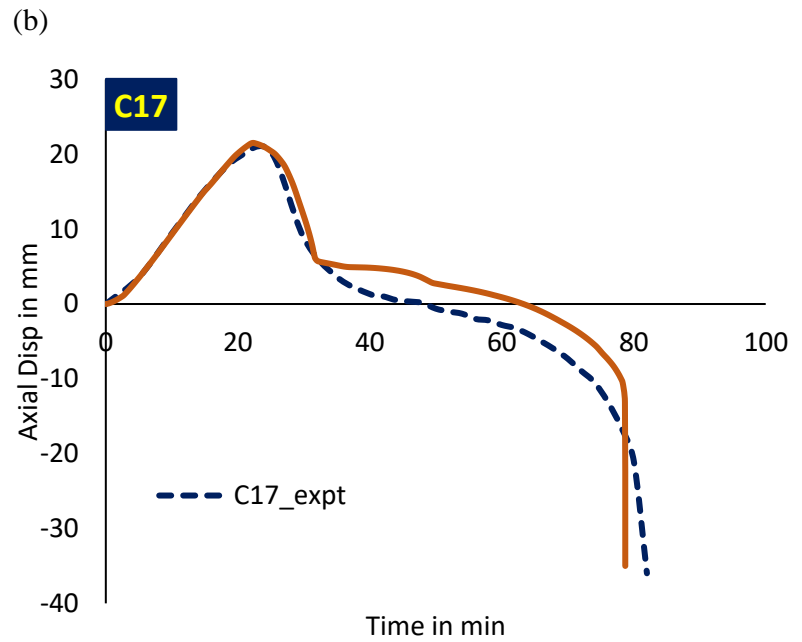
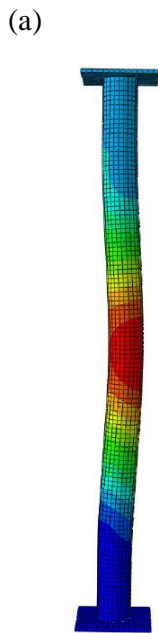
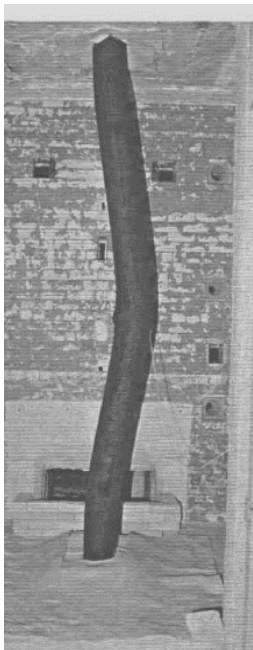


Figure 11 Deformed shape after exposure to standard fire, for column C-17

Figure 12 Comparison of axial displacement versus fire exposure time for experiment and predicted by simulation

The numerical model showed good agreement with the tests, as can be seen in Table 2. This table compares failure time in minutes obtained from the tests with the values predicted by means of the numerical model. The error is computed as the numerical (simulation) result divided by the experimental test result. It can be seen in Figure 13, most of the values lie in region of the 20% error, apart from two values, corresponding to columns no.30 and columns no. 60, which are relatively stocky columns.

| Sr. No. | Column no. | Relative slenderness ratio λ | Simulation Failure Time in min | Experimental Failure Time in min | Simulation Failure / Exp. Failure time |
|---------|------------|--------------------------------------|--------------------------------|----------------------------------|--|
| 1 | C-02 | 0.55 | 60 | 55 | 1.09 |
| 2 | C-04 | 0.55 | 59 | 57 | 1.04 |
| 3 | C-05 | 0.50 | 76 | 76 | 1.00 |
| 4 | C-06 | 0.70 | 45 | 60 | 0.75 |
| 5 | C-08 | 0.50 | 60 | 56 | 1.07 |
| 6 | C-11 | 0.40 | 63 | 80 | 0.79 |
| 7 | C-13 | 0.40 | 99 | 102 | 0.97 |
| 8 | C-17 | 0.37 | 79 | 82 | 0.96 |
| 9 | C-22 | 0.32 | 56 | 70 | 0.80 |
| 10 | C-23 | 0.28 | 163 | 143 | 1.14 |
| 11 | C-25 | 0.27 | 170 | 145 | 1.17 |
| 12 | C-26 | 0.26 | 102 | 93 | 1.10 |
| 13 | C-28 | 0.24 | 147 | 111 | 1.32 |
| 14 | C-29 | 0.22 | 204 | 170 | 1.20 |
| 15 | C-30 | 0.20 | 157 | 72 | 2.18 |
| 16 | C-53 | 0.26 | 142 | 149 | 0.95 |
| 17 | C-57 | 0.23 | 312 | 294 | 1.06 |
| 18 | C-59 | 0.20 | 157 | 125 | 1.26 |
| 19 | C-60 | 0.20 | 300 | 152 | 1.97 |
| | | Mean | 1.15 | Standard deviation | 0.36 |

Table 2-Results for validation columns from literature- Predicted and measured failure time.

Better match of simulation results was seen with the experiment for columns with smaller diameter, thus relatively slender columns for which mode of failure is buckling. However, the

columns with higher diameter produced more error, which can be due to the higher contribution of concrete and its more complex failure mechanisms.

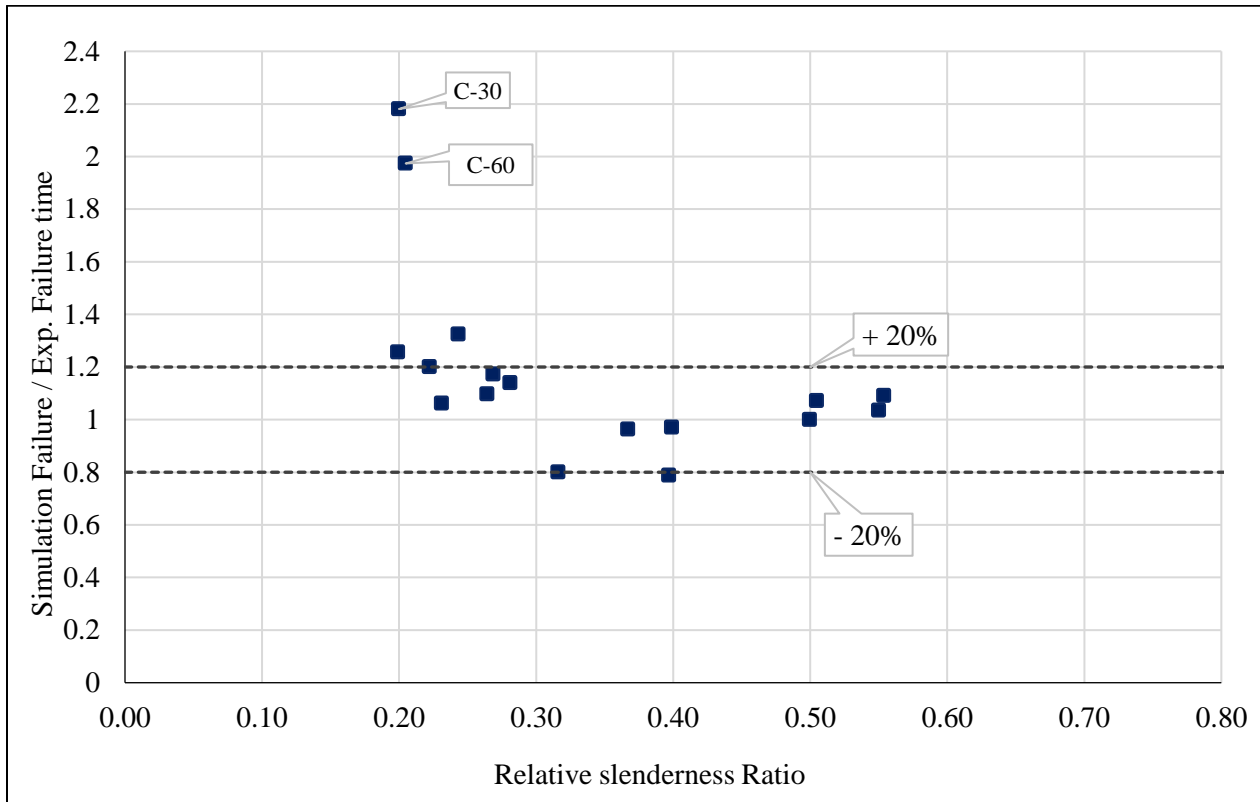


Figure 13-Comparison of error with calculated and measured failure time with relative slenderness ratio

Column C-06 is tested with pinned-pinned condition in test. However, the numerical model showed better agreement when the supporting conditions were considered as pinned-fixed. Three different supporting conditions were studied for simulating this pinned-pinned column and the results for the column is shown in Figure 14. It can be seen that the better prediction was obtained modelling the column as pinned-fixed.

As Renaud et al. already found it in the CIDECT research project 15Q, the reason of this behavior is that in real fire tests the unexposed ends of the column lying outside the furnace retain more stiffness, therefore introducing some rotational restraints to the column. In fact, the deformed shape of these column specimens after the tests suggests employing pinned-fixed supporting conditions when simulating their fire behavior.

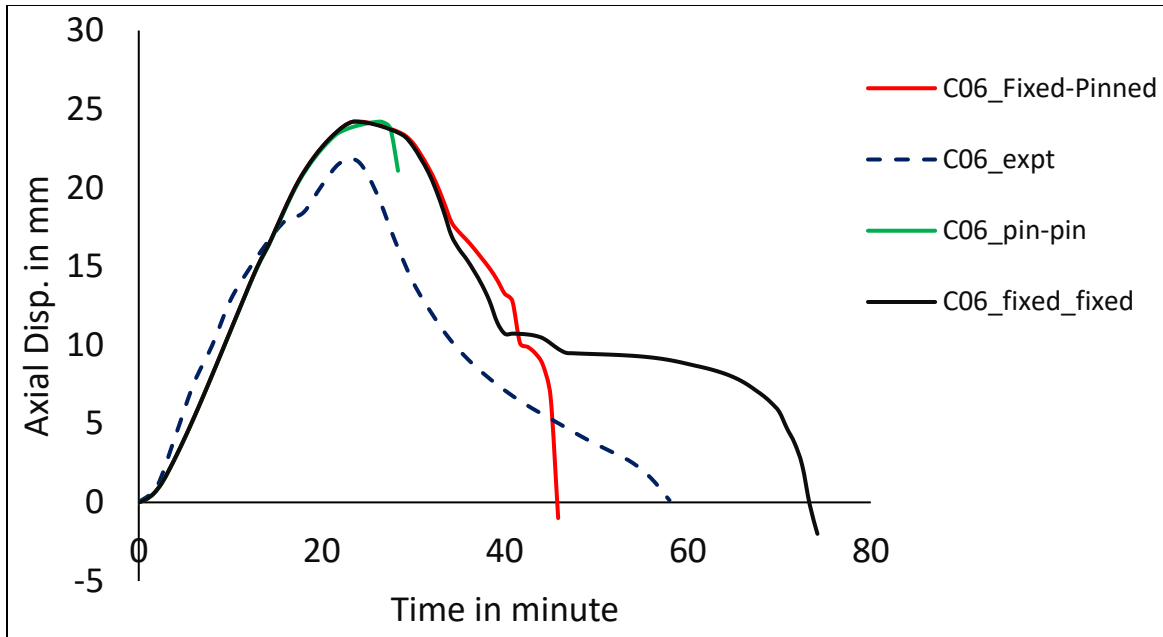


Figure 14-Comparison of different end conditions of column

To incorporate local imperfection of steel tube, higher Eigen-modes were given as initial geometric imperfection along with first buckling mode. Effect of two modes was negligible for columns with higher diameter but in case of slender columns failure time decreased by small amount. Figure 15 shows axial displacement versus failure time curve for column C-02 with different level of initial imperfection.

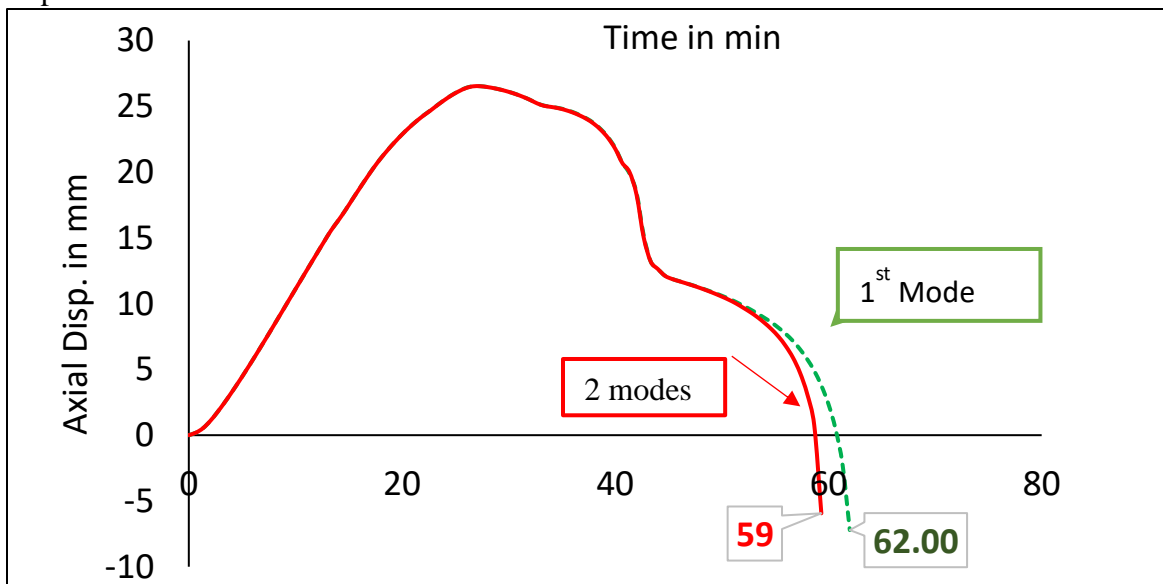


Figure 15-Comparison of different initial geometric imperfection on slender column

6. Validation of the FEM Model for CFT columns under Cyclic loading

To simulate and study the actual cyclic behavior of circular CFT columns, three-dimensional non-linear finite element analyses were conducted using the finite element software ABAQUS. For an accurate simulation, the nonlinear behavior of steel and concrete, the cyclic local buckling of steel tubes, the interface action between the concrete core and the steel tube and effect of end conditions were taken into consideration. The experimental work of Xiling Lu. et al was taken for validation of the model. Due to symmetry, only half of the column was modeled to simulate the effect of cyclic loading with one end of column keeping fixed and subjected to lateral load cycles while other end hinged and behavior of CFT is studied.

6.1. CFT columns details taken for validation under cyclic loading.

All specimens taken for validation are from experimental studies on square CFT columns under cyclic loading by Xilin LU and Weidong LU. They conducted cycled lateral load test on 11 CFT columns. The 1500 mm long column specimen was designed in accordance with the column part between the inflection point of top and bottom.

6.1.1. Dimensions and material properties

All 11 Square CFT specimens are 1500mm long and 200mm in width. Table 3Table 3 gives a list of specimen tested and the respective parameters. The steel tube was of mild steel of grade 16Mn (nominal yield stress $f_y=315$ MPa), and the nominal thickness of test specimens were 3 mm, 4 mm, and 5 mm. they have reported measured average f_{cu} and E_c values of concrete as $F_{cu} = 39.48$ MPa, 44.86 MPa and 48.07 MPa and $E = 35.36$ GPa, 35.31 GPa and 38.84 GPa for C40, C50 and C60 respectively.

Table 3- Test data of column specimens (Xilin Lu et al.)

| Specimen | D (mm) | Concrete Strength | t (mm) | n | Axial Load, N (KN) |
|----------|--------|-------------------|--------|-----|--------------------|
| R4M3 | 200 | C50 | 4 | 0.3 | 650 |
| R4M5 | 200 | C50 | 4 | 0.5 | 1100 |
| R4M7 | 200 | C50 | 4 | 0.7 | 1550 |
| R4L5 | 200 | C40 | 4 | 0.5 | 1050 |
| R4L7 | 200 | C40 | 4 | 0.7 | 1450 |
| R4H5 | 200 | C60 | 4 | 0.5 | 1150 |

| | | | | | |
|------|-----|-----|---|-----|------|
| R4H7 | 200 | C60 | 4 | 0.7 | 1600 |
| R5M5 | 200 | C50 | 5 | 0.5 | 1200 |
| R5M7 | 200 | C50 | 5 | 0.7 | 1680 |
| R3M5 | 200 | C50 | 3 | 0.5 | 950 |
| R3M7 | 200 | C50 | 3 | 0.7 | 1350 |

6.1.2. Test set up

Schematic representation of the test specimen is shown in Figure 16. Test setup provides cylinder hinged support at top and bottom ends. Axial Load was applied to the bottom of the specimen and the lateral load was applied in the middle of the specimen. Axial load, N was applied as compressive force ratio $n=N/N_0$, where N_0 is equal to total nominal collapse load capacity of the specimen, the values listed in Table 3

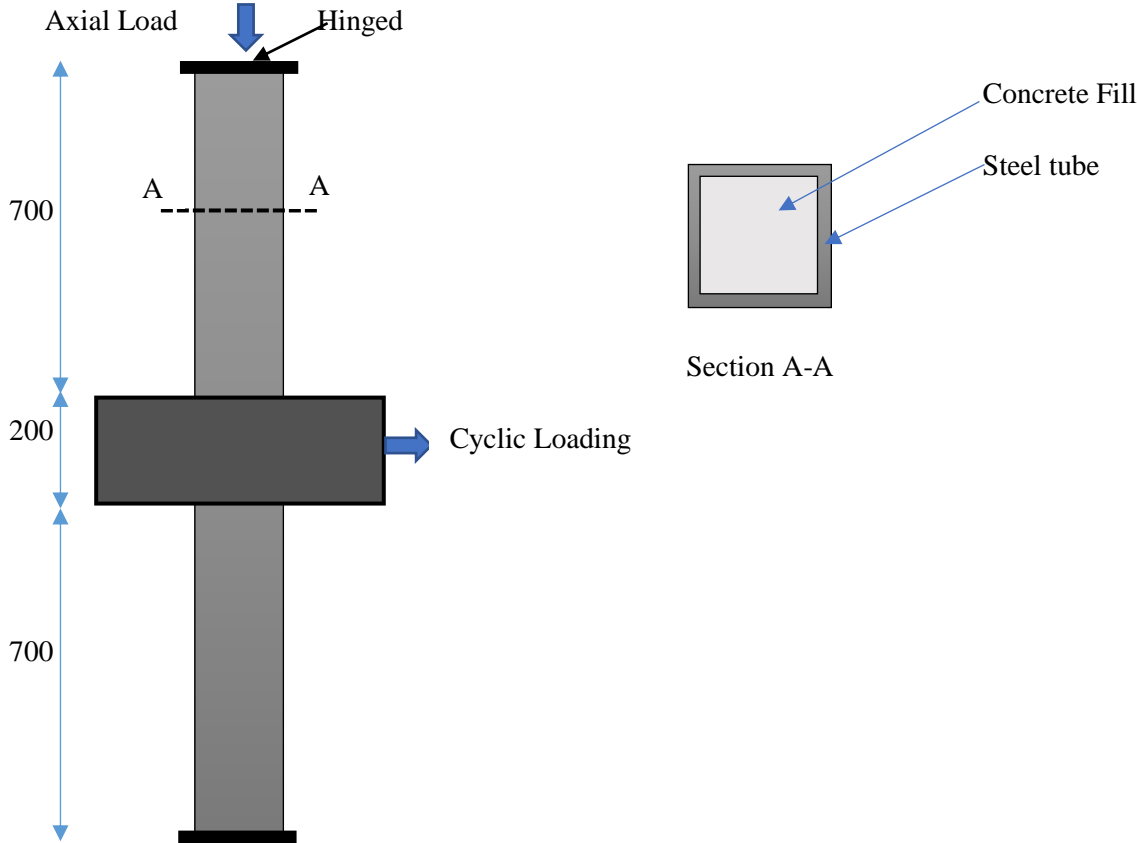


Figure 16- Test Setup (Xilin Lu et al.)

Displacement History

All 11 specimen were subjected to lateral loading cycles as shown in Figure 17 under constant axial load N . Peak displacements (δ) were increased stepwise after three successive cycles at each displacement level in a ratio of yield displacement(δ_y).

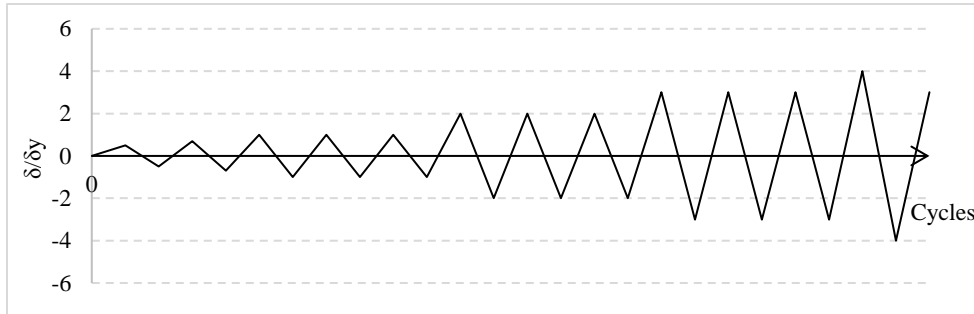


Figure 17-Displacement history as per experiment

6.1.3. Results and discussion of Test data.

All specimens were failed in same collapse mode, buckling of the column with higher axial load ratio was seen earlier than lower load ratio, also specimens with 3 mm plate thickness buckled locally more than with thickness of 4 and 5 mm. Figure 18 shows the failure of one of the specimens- R3M7.



Fig.4 R3M7 after failure
Failure



Fig.5 Typical concrete failure
Appearances of Filled-in Concrete

Figure 18-Failure of specimen- R3M7

The typical horizontal load versus horizontal displacement hysteretic curves for the test specimens from experiments are shown in graphs attached in the Annexure. Results from cycling loading test on the 11 CFT specimens is summarised in below Table 4.

Notation Used in Table is, $n=N/N_0$ is the compression force ratio; Q_{ul} and Q_{ur} are the lateral loads when specimen reaching ultimate load in positive cycles and negative cycles

Table 4- Result Summary of experiments (Xilin Lu et al.)

| No. | Specimen | F_{cu} (MPa) | n | N (KN) | Q_{ul} (KN) | Q_{ur} (KN) |
|-----|----------|----------------|-----|----------|---------------|---------------|
| 1 | R3M5 | 44.9 | 0.5 | 950 | -292.9 | 280.4 |
| 2 | R3M7 | 44.9 | 0.7 | 1350 | -230.4 | 238.9 |
| 3 | R5M5 | 44.9 | 0.5 | 1200 | -353.1 | 375.3 |
| 4 | R5M7 | 44.9 | 0.7 | 1680 | -340.5 | 321.7 |
| 5 | R4L5 | 39.5 | 0.5 | 1050 | -316.8 | 313.1 |
| 6 | R4L7 | 39.5 | 0.7 | 1450 | -284.5 | 305.1 |
| 7 | R4M3 | 48.1 | 0.3 | 1150 | -283.6 | 305.2 |
| 8 | R4M5 | 48.1 | 0.5 | 1600 | -309.7 | 321 |
| 9 | R4M7 | 44.9 | 0.7 | 650 | -250.2 | 277.8 |
| 10 | R4H5 | 44.9 | 0.5 | 1100 | -385 | 366 |
| 11 | R4H7 | 44.9 | 0.7 | 1550 | -346 | 337 |

6.2. Procedure of simulation for cyclic loading

As shown in Figure 19, only half of the column length i.e. 700 mm is modeled in the present study. At one end axial load (N) is kept constant and with varying lateral cyclic loading as well, while another end is kept hinged.

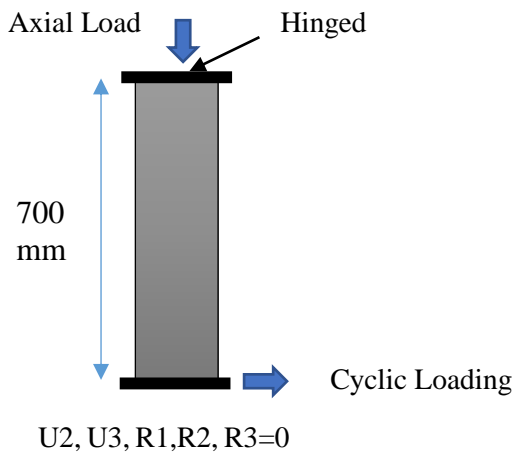


Figure 19- Representation of FEM model

In experiments, lateral displacements are given at mid-level of the column. As only half of the column is modeled in present validation, fully reverse displacement cycles as shown in fig. were

given to columns as displacement boundary condition at one end of the column keeping under end hinged as the experimental setup. Peak displacements (δ) were increased stepwise after three successive cycles at each displacement level in a ratio of yield displacement(δ_y). The analysis was conducted in displacement control mode.



Elastic and plastic material properties for steel and concrete models are taken from Euro code. For Steel simple bilinear kinematic hardening model was implemented. And strain hardening rate was considered to be 1% of the initial elastic stiffness of the steel material. Concrete was modeled using the Damaged Plasticity model. Stress-Strain relationship used for concrete and steel in the FEM model is discussed in the Annexure.

The two-step explicit analysis was performed for studying the behavior of CFT columns cyclic loading. In the first step, the axial load was applied by a gradual increment in two seconds and later the load was kept throughout the analysis. In second-step, cyclic lateral displacement was applied.

6.3. Validation Results

Qul and Qur values obtained from the analysis are shown in the following table and compared with experimental data. Where Qul and Qur are the lateral loads when specimen reaching ultimate load in positive cycles and negative cycles. The graph in Figure 20 (a) and (b) in and shows the comparison of numerically obtained lateral force versus displacement curve with experiments for R3M5 and R3M7 columns. And lateral force versus displacement hysteresis curve for remaining columns are shown in Figure 21.

Table 5- Results from validation of CFT columns under cyclic loading

| All values in KN | | | Experiment Results | | Analysis Results | | Expt. /Analysis lateral load | |
|------------------|--------|---------|--------------------|-------|------------------|-----|------------------------------|----------|
| | Sp.No. | n= N/N0 | Qul | Qur | Qul | Qur | Qul | Qur |
| 1 | R3M5 | 950 | -292.9 | 280.4 | -230 | 226 | 0.785251 | 0.805991 |
| 2 | R3M7 | 1350 | -230.4 | 238.9 | -200 | 198 | 0.868056 | 0.828799 |
| 3 | R5M5 | 1200 | -353.1 | 375.3 | -290 | 296 | 0.821297 | 0.788702 |
| 4 | R5M7 | 1680 | -340.5 | 321.7 | -224 | 216 | 0.657856 | 0.671433 |
| 5 | R4L5 | 1050 | -316.8 | 313.1 | -258 | 246 | 0.814394 | 0.785691 |
| 6 | R4L7 | 1450 | -284.5 | 305.1 | -206 | 210 | 0.724077 | 0.688299 |
| 7 | R4M3 | 1150 | -283.6 | 305.2 | -294 | 300 | 1.036671 | 0.982962 |
| 8 | R4M5 | 1600 | -309.7 | 321 | -246 | 244 | 0.794317 | 0.760125 |
| 9 | R4M7 | 650 | -250.2 | 277.8 | -206 | 186 | 0.823341 | 0.669546 |
| 10 | R4H5 | 1100 | -385 | 366 | -296 | 278 | 0.768831 | 0.759563 |
| 11 | R4H7 | 1550 | -346 | 337 | -314 | 286 | 0.907514 | 0.848665 |

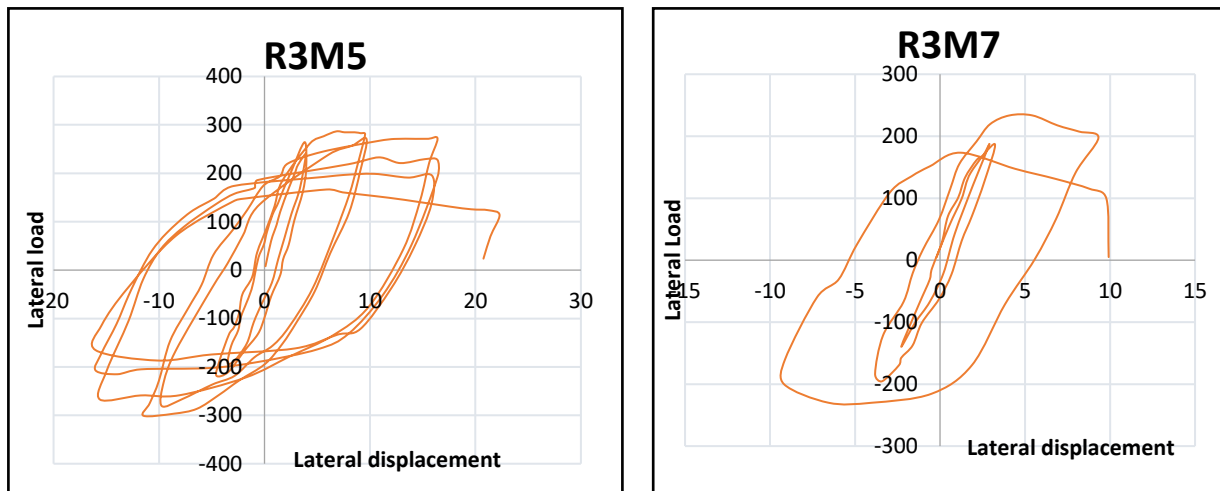
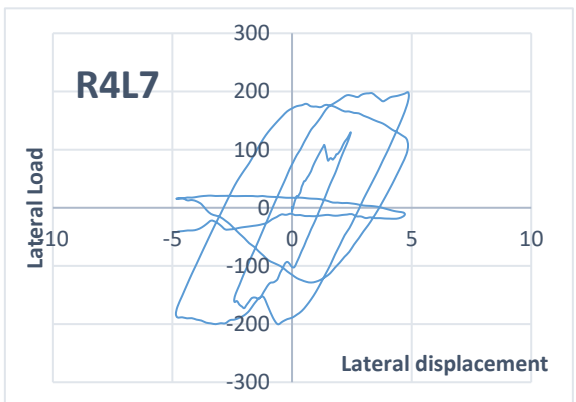
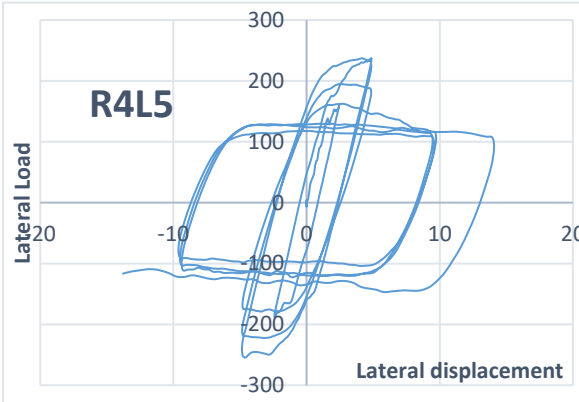
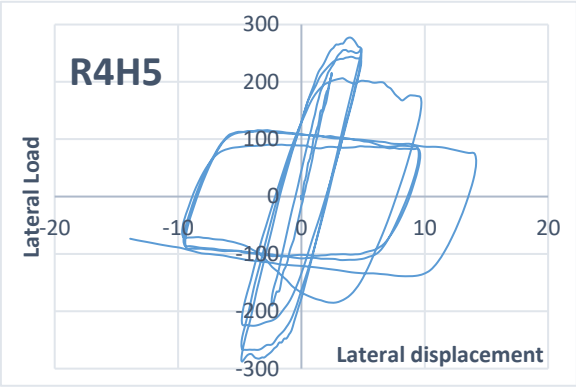
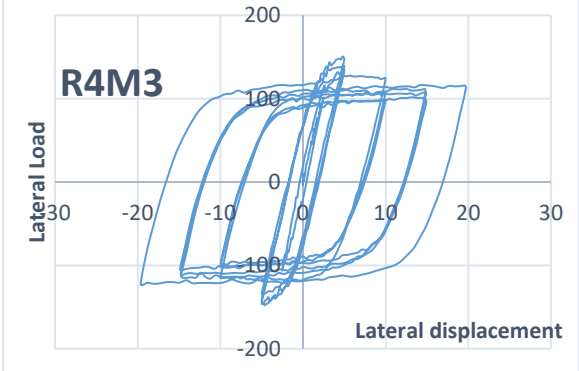
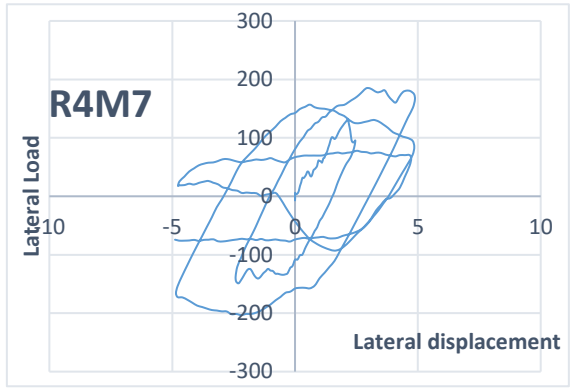
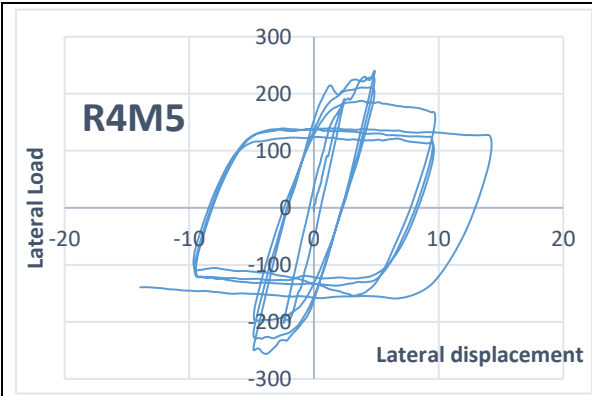


Figure 20- Comparison of simulated lateral force versus displacement curve with experiments



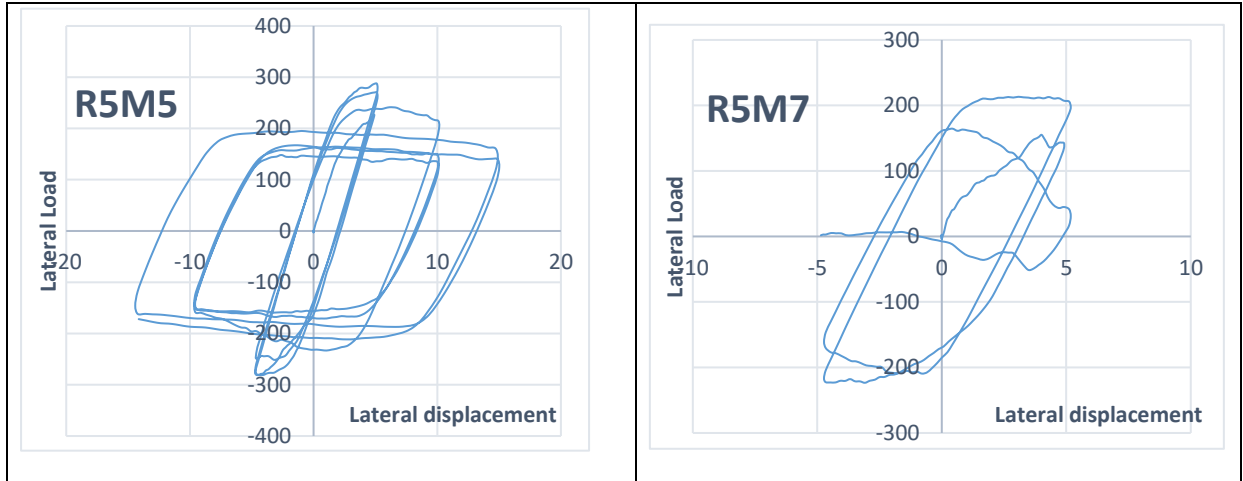


Figure 21-Horizontal load versus horizontal displacement- hysteretic curves for simulated columns

Following plot compares experimental results with results obtained from ABAQUS model.

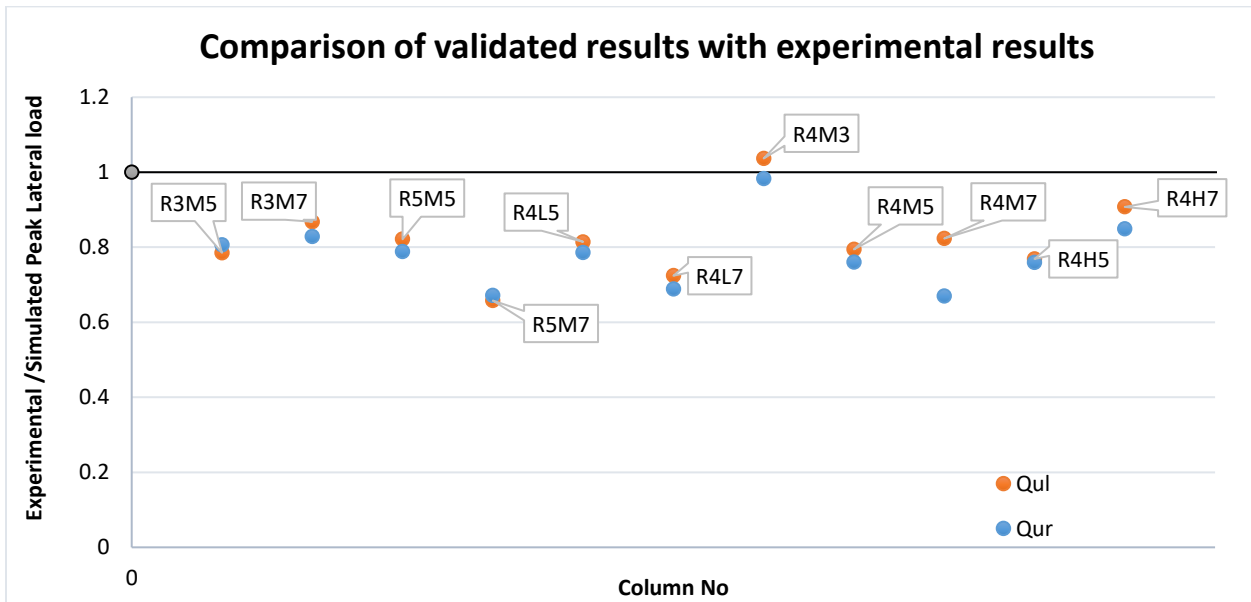


Figure 22- Comparison of validated results with experimental results

6.3.1. Effect of the bond between steel tube and concrete

There is possibility of some chemical bond between steel tube and concrete in the initial stage of cyclic loading. In the later stages, bond will be lost due to local buckling of steel tube and concrete cracks. Bond between steel and concrete may affect behavior of CFT columns under cyclic loading.

The previously validated models for CFT columns under cyclic loading was checked again by proving perfect bond between steel tube and concrete core (Tie Module in ABAQUS). It is found that bond increases initial lateral load capacity of the columns.

Figure – 24 shows that in initial cycles fully bonded condition gives higher peak load capacity than without bond condition.

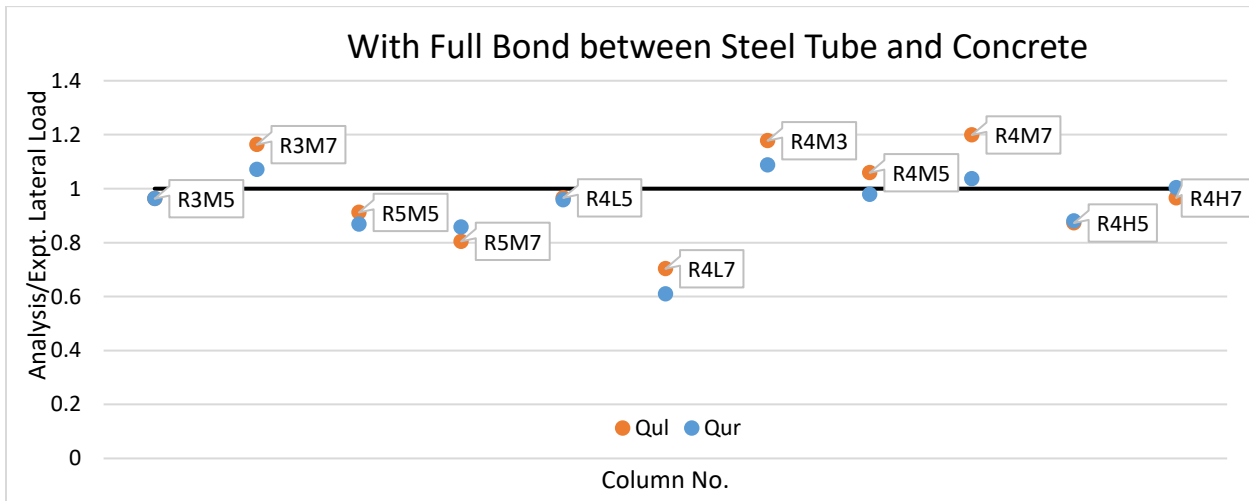


Figure 23- Effect of perfect bond between steel and concrete on peak lateral load

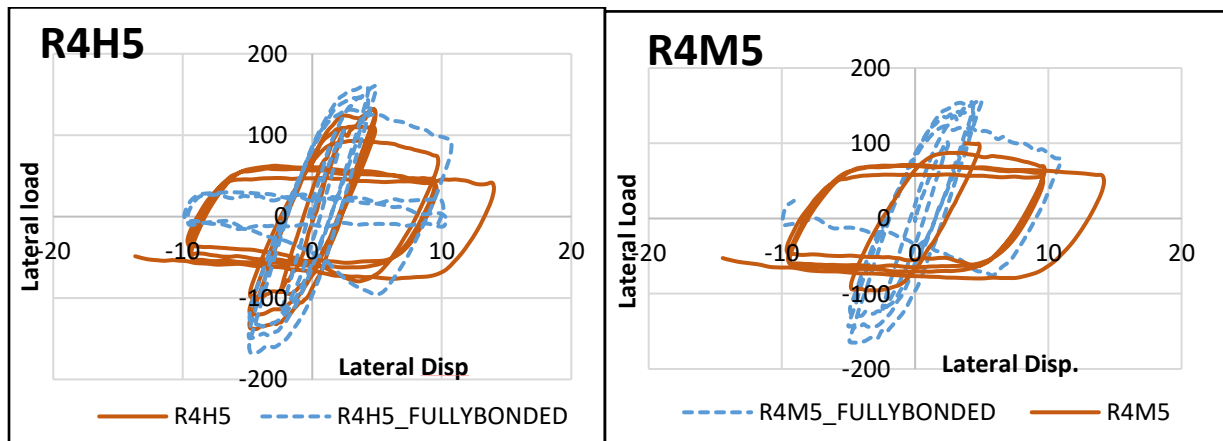


Figure 24- Comparison with addition of perfect bond

6.3.2. Effect of end condition- the addition of rotational stiffness and fixity

Experimental set up says that cylindrical hinge support is provided at one end of column. But there is possibility of support giving some rotational restraint to the columns. To check the effect of rotational-restrain, some restrain is added at the boundary in the terms of multiple of elastic rotational stiffness (K) of the respective columns. Following tables gives the respective initial elastic rotational stiffness value of the columns and effect was checked for 1.5 times, 15 times and 20 times K value. Also the fixed end condition is used to check effect.

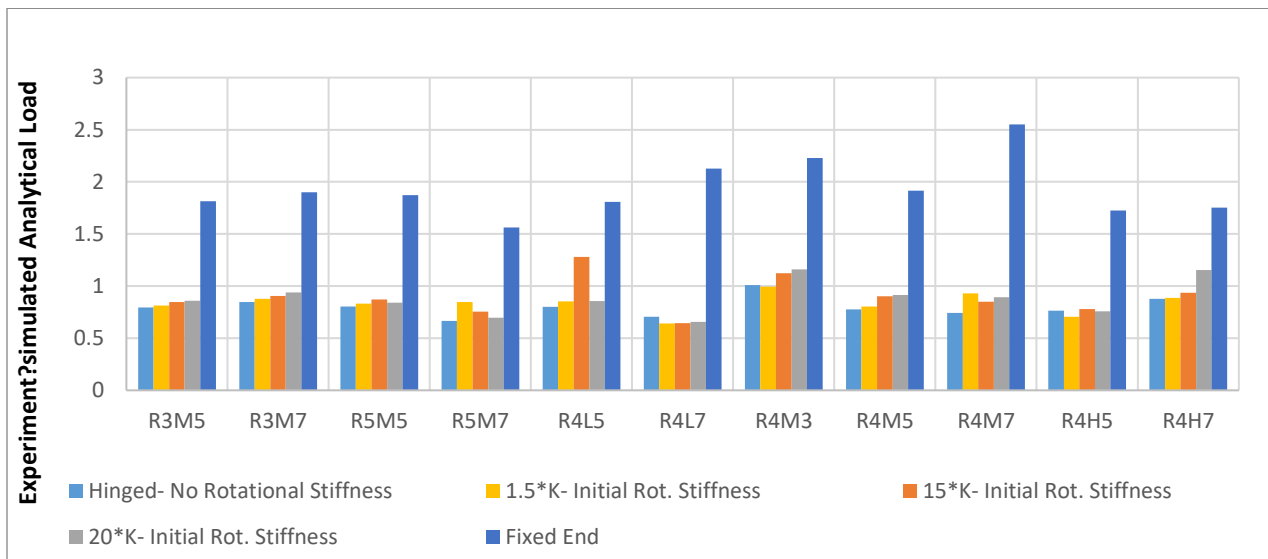


Figure 25- Effect of end restrains

It can be seen that there is very minute effect of rotational effect on the lateral load capacity of column. But the capacity almost doubles because of fixity.

7. Finite element simulation of Post-Earthquake Fire scenario for CFT column

This section investigates the behavior of CFT columns under post-earthquake fire scenario. In previous sections (5) and (6), models were developed to study the behavior of CFT column under cyclic loading and fire under constant axial loading respectively. Models were already validated with available experimental data for both conditions. So same material models and analysis procedure is adopted to study behavior CFT columns under Post-Earthquake Fire scenario.

7.1. Details of specimens under study

To study the behavior of CFT column under Post-Earthquake Fire scenario, axially loaded columns validated under fire exposure from NRCC report in the section was taken. As Experimental data of CFT columns under post-earthquake fire was unavailable, columns of NRCC Report are taken for this studies. 6 columns with varying relative slenderness ratio and dimension were taken for examining the effect of slenderness on the extent of damage due to cyclic loading and time of failure under post-earthquake fire condition. Out of 6, 3 were a circular column and remaining 3 were square. Test details of columns under study is shown in Table 6. All columns tested were of 3810 mm length.

Table 6-Details of CFT columns under the study of post-earthquake fire scenario

| Column No. | Dia./Width (mm) | Wall Thick. (mm) | Concrete Strength (MPa) | Yield Strength (MPa) | Test load (KN) |
|------------|-----------------|------------------|-------------------------|----------------------|----------------|
| C-05 | 168.3 | 4.78 | 32.7 | 350 | 150 |
| C-17 | 219.1 | 8.18 | 31.7 | 350 | 525 |
| C-26 | 323.9 | 6.35 | 24.3 | 350 | 1050 |
| | | | | | |
| SQ-01 | 152.4 | 6.35 | 58.3 | 350 | 376 |
| SQ-20 | 254 | 6.35 | 58.3 | 350 | 931 |
| SQ-24 | 304.8 | 6.35 | 58.3 | 350 | 1130 |

7.2. Element and Material model.

Element type for concrete and steel is kept same as an earlier validated model for cyclic loading and fire test. C3D8R- 8 noded solid elements with reduced integration are used for modeling concrete core and S4R- 4-noded shell element is used for modeling steel tube. Elastic-Linear

plastic material properties were used for steel material with kinematic linear plastic hardening model. For modeling concrete material, concrete damage plasticity model was used because of its ability to capture damage in cyclic loading step. All material properties were taken from Eurocode for fire-design, (EN 1994-1-2, Euro-code 4). Stress-Strain relationship of steel and concrete material at a different temperature is discussed in Annexure. Thermal Properties for steel and concrete were kept as a validated model in section 5 and taken from EUROCODE-2.

7.3. Step-wise procedure for analysis

For studying the fire resistance of damaged column after cyclic loading under fire, 3 step non-linear stress – explicit analysis was performed. Heat transfer analysis was performed on the full length of column unlike experiments of NRCC report because the effect of damage due to the earthquake is major at the connection level. To study post-earthquake fire resistance of CFT columns its necessary to expose ends of the column to fire to capture more realistic scenario. Different damage level (moderate to high) was introduced to examine the effect of damage and strength reduction.

Cyclic Analysis

The cyclic analysis is the same as discussed in section 6. Cycling loading was applied to columns with the content initial axial load. All columns were analyzed for the different level of percentage drift (max. horizontal displacement at end/length of the column). Displacement history is given based on ATC-24 recommendations (ATC 24). First yield displacement of the column was determined by subjecting column to cycles of increasing amplitude of displacements up to the point when columns start showing plastic strains in a steel tube. Yield displacement means the displacement level at which outer steel tube starts yielding. After estimation of yield displacement, columns were subjected to a different number of cycles, so that maximum displacement for different cycles are multiples of estimated yield displacement. Different damage levels were created in columns to study the effect.

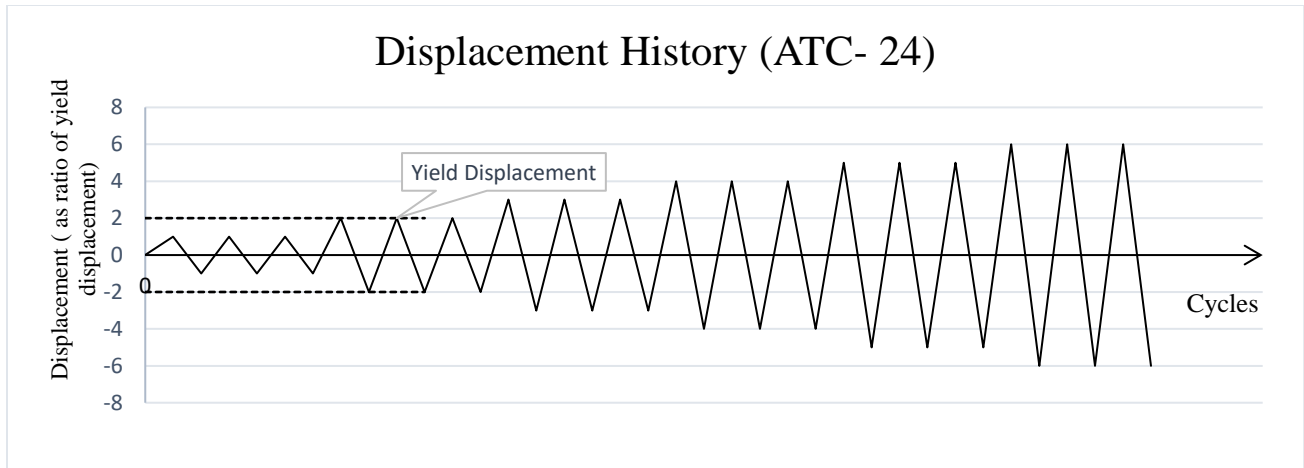


Figure 26- Displacement history according to ATC- 24 recommendation

The release of lateral force after cyclic loading

Lateral force of reaction is generated at the end of the cyclic loading step due to the presence of drift. This force is released by removing all lateral displacement (drift), maintaining residual drift as it is. In real earthquake scenario usually all horizontal reaction forces are release after shaking, but permanent drifts are damage remains in building depending upon the type of earthquake (moderate or high).

Heat Transfer Analysis

A transient heat transfer analysis was conducted on all specimens under the study to simulate the effect of ASTM E119 standard fire applied to the full length of the column. The recorded nodal time- Temperature curves for the steel-concrete model was provided as input in Heat-Step. The preliminary finite element analysis of heat transfer procedure discussed in section 5 showed acceptable match of Time-Temperature history with experimental data. Procedure for heat transfer analysis to get nodal temperature history is same as earlier. Heat transfer element type was used for concrete and steel tube.

Stress/deformation analysis for damaged columns

In this step nodal time history of temperature from the previously generated heat transfer file was applied to the damaged column. The model generated for heat transfer analysis is modified for stress analysis keeping number of mesh size (nodes and element) same. The first cyclic analysis was performed on the column to create desired damage (drift). The release of lateral forces gives

a stress-free model which have only residual because of cyclic loading. After that, two-step thermal-stress analysis (Force- controlled axial loading and fire loading) was performed on the column to simulate the scenario of post-earthquake fire.

Same columns were analyzed under purely axially loaded condition (without any cyclic loading) to compare the time of failure with and without damage.

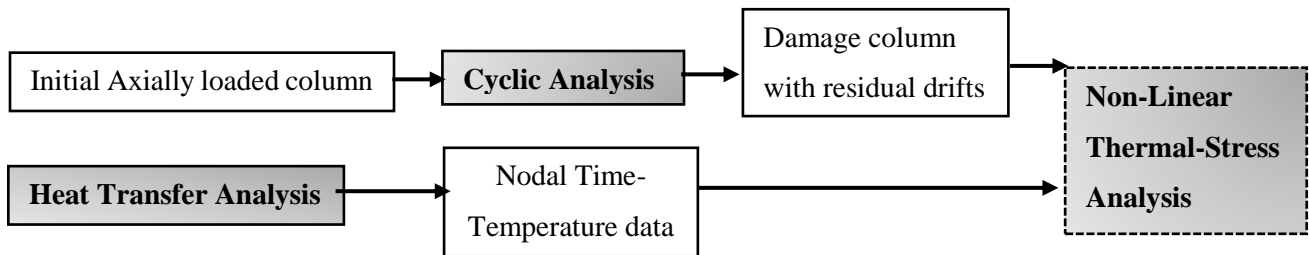


Figure 27-Scheme of analysis

8. Results and discussions.

This section examines the effect of damaged due to a different level of drifts due to cyclic loading on fire resistance capacity of CFT column. All columns mention in the Table 6 were subjected to a different percentage of drift and peak lateral displacements in terms of yield displacement of steel tube, to study the effect. The first cyclic analysis was performed on columns for finding out the lateral displacement at which steel tube yields by subjecting displacement cycles recommended by ATC-24. After finding the yield-displacement, cycles were given in multiples of that yield displacement.

In below section, results from the analysis of all 6 columns under study are discussed concisely through the axial displacement-time responses predicted by the finite element models in non-linear thermal stress analysis phase. Also, residual drifts remained in the column at the end of each cyclic loading are tabulated for discussion. Drift_ratio for each case is mentioned as the ratio of maximum peak displacement of loading cyclic to the length of the column.

Column No – C05

This is a slender circular column with relative slenderness ratio of 0.49 and L/d ratio of 22.6.

Yield displacement of the column is 50 mm.

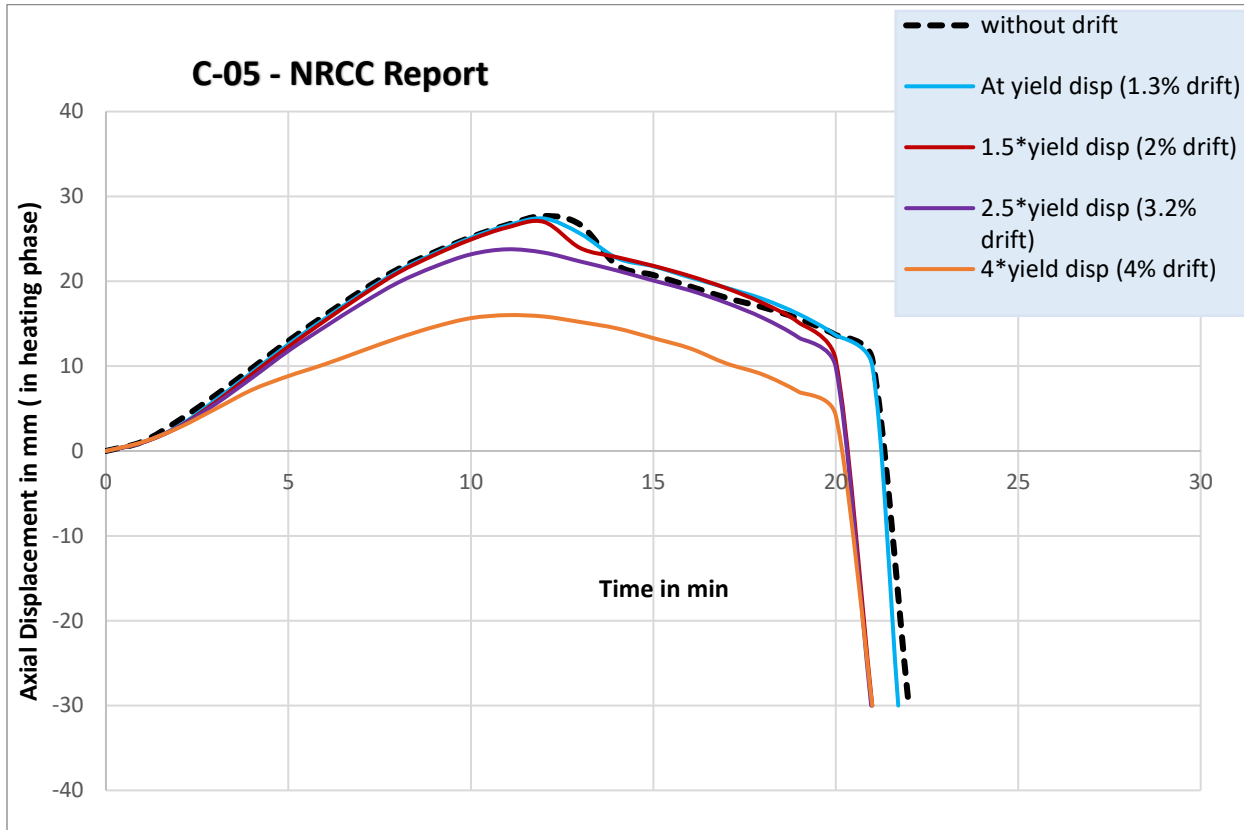


Figure 28- C-05 Axial displacement vs time of exposure for different damage level

| Max. Drift | Max peak lateral disp. Applied during a cyclic step in mm | Residual drift remaining at the onset of heat analysis | Time of failure after fire loading in min |
|------------|---|--|---|
| 4 % | +/-150 | -95 | 21 |
| 3.2% | +/-125 | -80 | 21 |
| 2% | +/-90 | -37 | 21 |
| 1.3% | +/-50 | -10 | 22 |
| No Drift | 0 | 0 | 22.5 |

Table 7- Test Result C-05

Column No – SQ-01

This is a slender circular column with an L/d ratio of 25.

Yield displacement of the column is 37 mm.

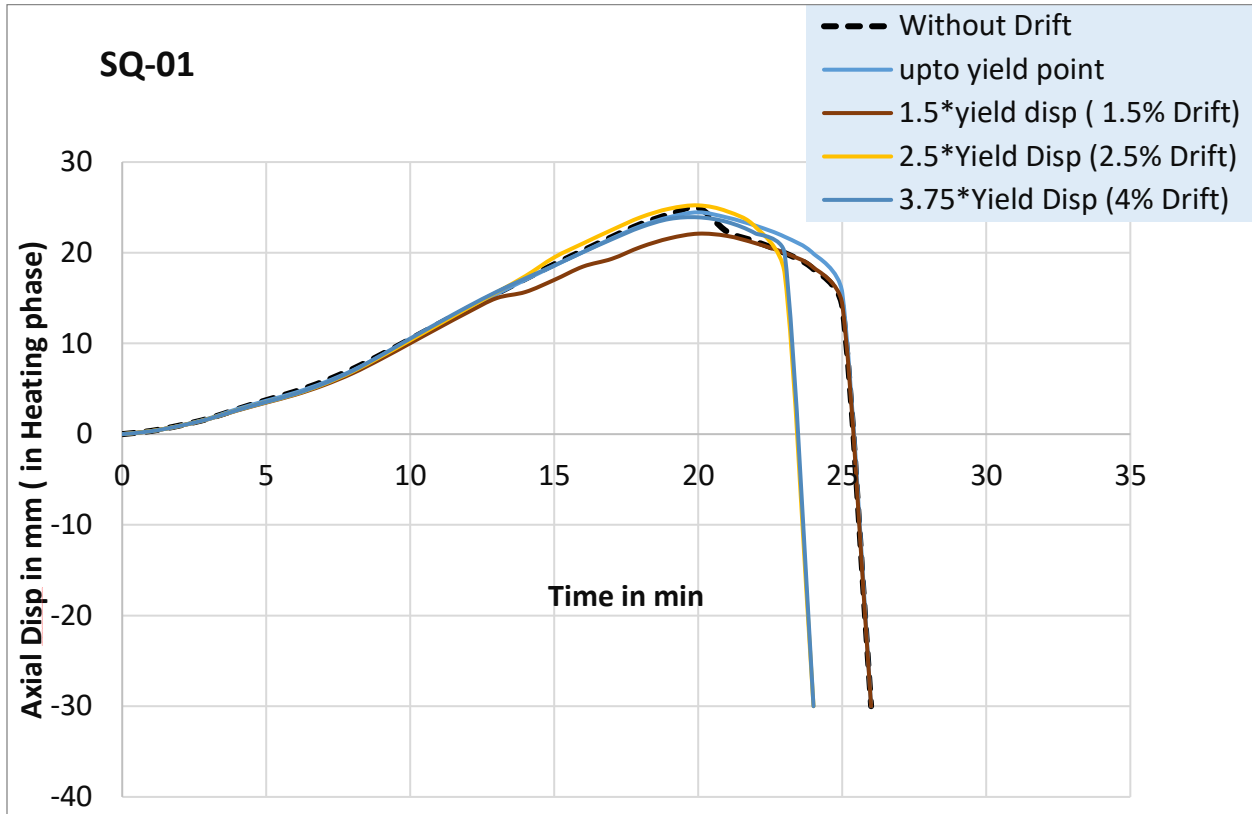


Figure 29 SQ-01- Axial displacement vs time of exposure for different damage level

| Max. Drift | Max peak lateral disp. applied during a cyclic step in mm | Residual drift remaining at the onset of heat analysis | Time of failure after fire loading in minutes |
|------------|---|--|---|
| 3.75% | +/-150 | -77 | 24 |
| 2.5% | +/-100 | -37 | 24 |
| 1.5% | +/-60 | 21 | 26 |
| 1% | +/-40 | 20 | 26 |
| No drift | 0 | 0 | 26 |

Table 8-Test Result SQ-01

Column No.- C-26

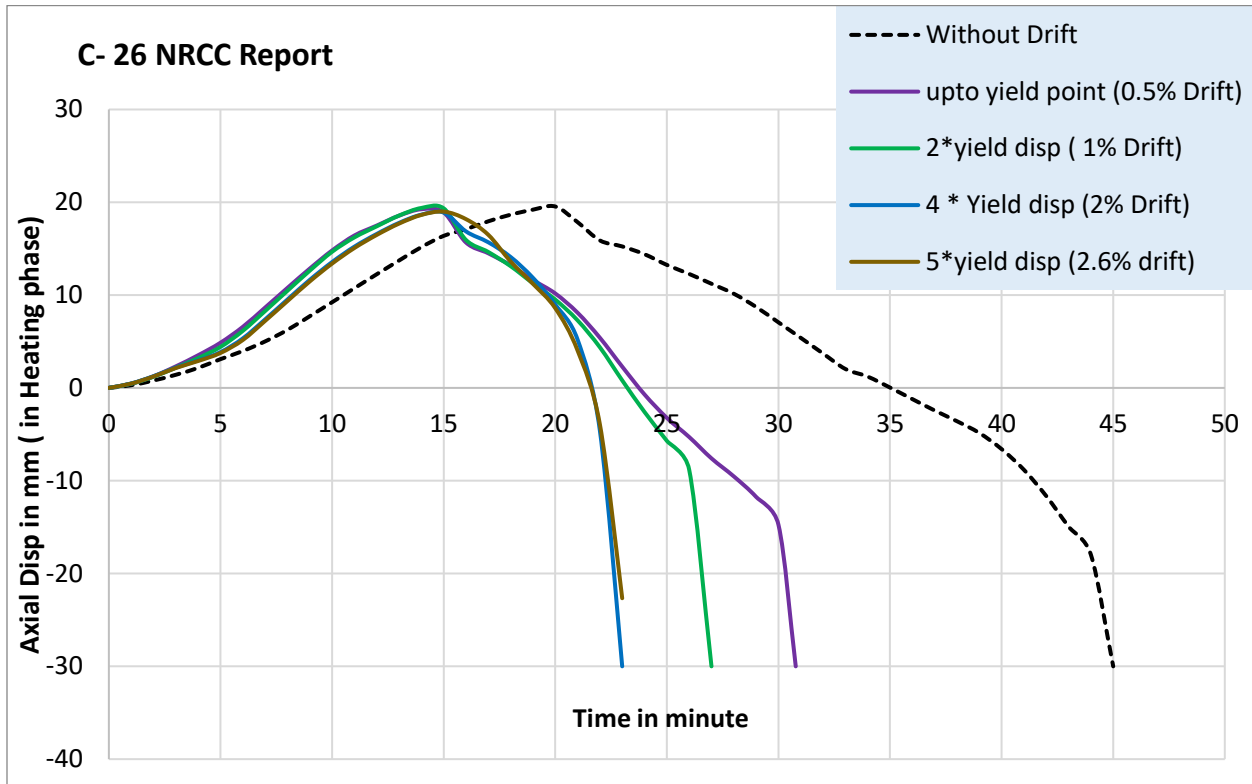


Figure 30 C-26- Axial displacement vs time of exposure for different damage levels

| Max. Drift | Max peak lateral disp. Applied during a cyclic step in mm | Residual drift remaining at the onset of heat analysis | Time of failure after fire loading in min |
|------------|---|--|---|
| 4 % | +/-150 | -95 | ABAQUS error due steel element failure |
| 2.6% | +/-100 | -37 | 23 |
| 2% | +/-80 | -21 | 23 |
| 1% | +/-40 | -10 | 23 |
| 0.5% | +/-20 | -8.45 | 31 |
| No Drift | 0 | 0 | 45 |

Table 9-Test Result C-26

Column No - SQ-20

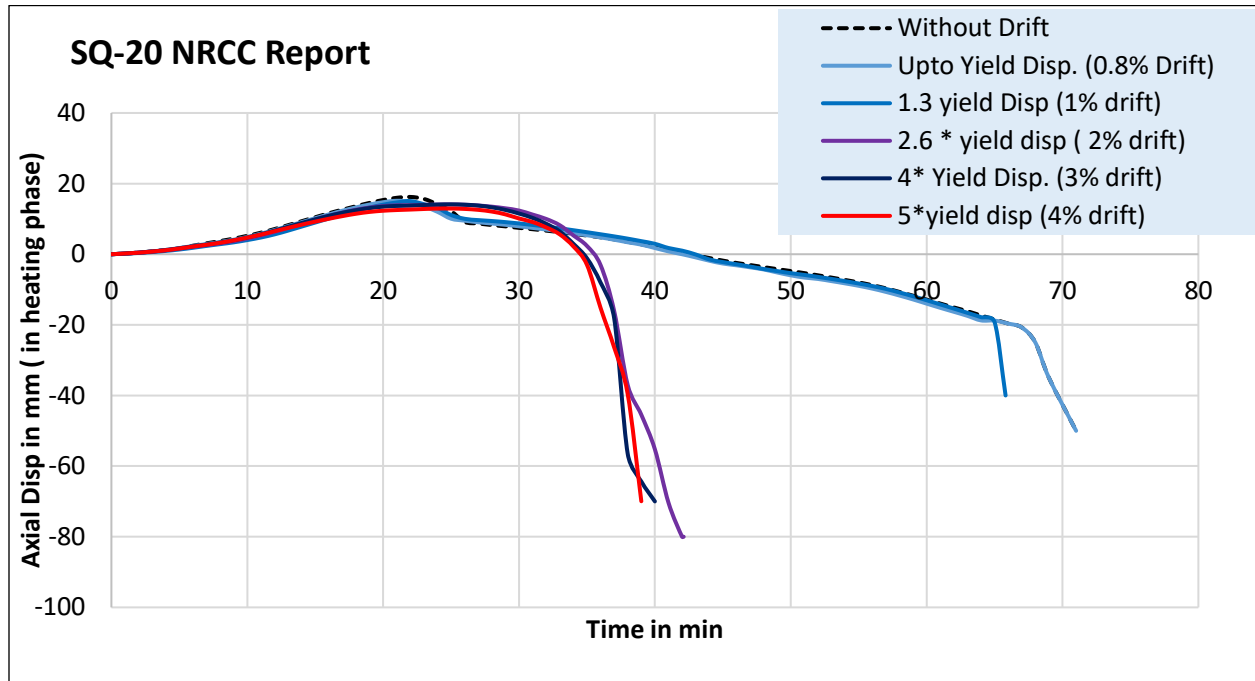


Figure 31 SQ-20 Axial displacement vs time of exposure for different damage levels

| Max. Drift | Max peak lateral disp. Applied during a cyclic step in mm | Residual drift remaining at the onset of heat analysis | Time of failure after fire loading in min |
|------------|---|--|---|
| 4 % | +/-150 | -100 | 39 |
| 3% | +/-120 | -80 | 40 |
| 1.5% | +/-80 | -47 | 43 |
| 1% | +/-40 | 15 | 65 |
| 0.8% | +/-30 | 10 | 71 |
| No Drift | 0 | 0 | 71 |

Table 10-Test Result SQ-20

Column No- SQ-24

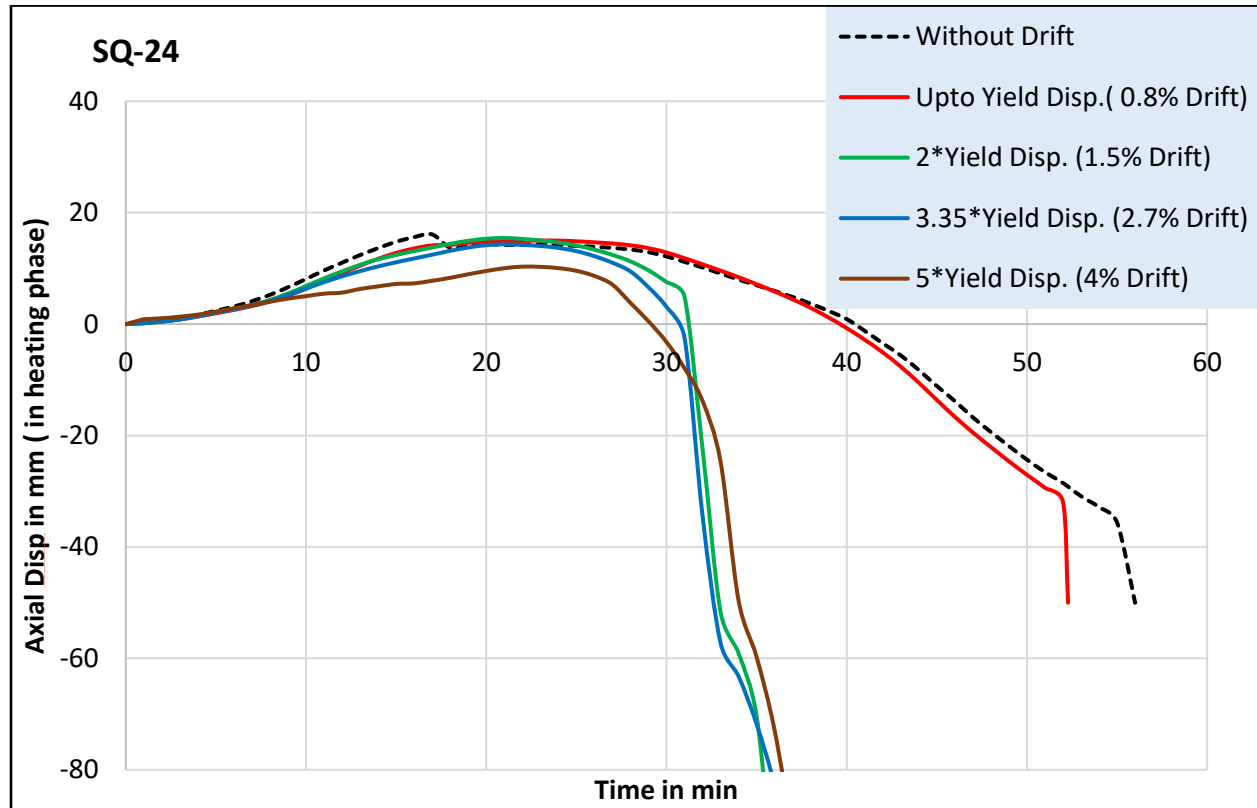


Figure 32 SQ-24 Axial displacement vs time of exposure for different damage levels

| Drift Ratio | Max peak lateral disp. Applied during a cyclic step in mm | Residual drift remaining at the onset of heat analysis | Time of failure after fire loading in min |
|-------------|---|--|---|
| 4 % | +/-150 | -106 | 37 |
| 2.6% | +/-100 | -60 | 37 |
| 1.5% | +/-60 | -30 | 37 |
| 0.8% | +/-30 | -7.2 | 52 |
| No Drift | 0 | 0 | 57 |

Table 11-Test Result SQ-24

Discussion.

From the graphs, it can be seen that when the column is subjected to peak lateral displacement equal to yield displacement of a steel tube or also if residual deformation after cyclic loading is less than yield displacement, the time of failure of CFT columns in fire event remains same as an undamaged column. While as the drift ratio increases, column fails little earlier than the undamaged column, this can be attributed to residual displacement in damage column, which initiate buckling of column early. Also, the strength of column decreases as drift ratio increases. However, in slender columns failure is governed by elastic- plastic buckling of column, so the failure time is almost same as undamaged one as degradation in strength is not governing factor for the slender column. While in case of stocky columns C-26, SQ-20 and SQ-24, residual drift plays an important role for fire resisting capacity.

In case C-26 column, axial load applied is 1.16 times concrete core capacity. So even if column is subjected low damage level as in case of peak lateral displacement equal to equal to yield displacement, reduction in strength of concrete core will be there and may not be able to sustain fire load for long time (as steel is already failed in initial time of fire). So failure is 15 mins early than undamaged columns.

However, SQ20 AND SQ24, axial load applied is 0.8 times concrete core capacity, so even when peak lateral displacement in cyclic phase is equal to or slightly more than yield displacement, damage may not cause early failure, as concrete can still take load even steel is failed. However, as lateral displacement increases, damage in concrete also increases and strength reduces. Moreover, damaged columns will not take load in fire and fails early.

9. References

1. ABAQUS Standard User's Manual, The Abaqus Software is a product of Dassault Systèmes Simulia Corp., Providence, RI, USA Dassault Systèmes, Version 6.14.1, USA; 2013
2. AISC (2010), *Draft Specification for Structural Steel Buildings*, ANSI/AISC 360-10, American Institute of Steel Construction, Inc., Chicago, IL. August 3rd, 2009.
3. Ana Espinos, Manuel L. Romero, Antonio Hospitaler, "Advanced model for predicting the fire response of concrete filled tubular columns", *Journal of Constructional Steel Research*
4. ATC (1992), *ATC-24 Guidelines for Testing Steel Components*, Applied Technology Council, Redwood City, CA.
5. CEN. EN 1994-1-1, Eurocode 4: Design of composite steel and concrete structures. Part 1-1: General rules and rules for building.
6. CEN. EN 1994-1-2, Eurocode 4: Design of composite steel and concrete structures. Part 1-2: General rules – Structural fire design. Brussels, Belgium: Comite Europeen de Normalisation; 2005.
7. Charles Schencking, *The Great Kantō Earthquake and the Chimera of National Reconstruction in Japan*.
8. Chithira, K. and Baskar, K., "Experimental Investigation on Circular CFT columns with and without shear connectors"
9. Ding J, Wang YC. Realistic modelling of thermal and structural behaviour of unprotected concrete filled tubular columns in fire. *Journal of Constructional Steel Research* 2008;64:1086_102.
10. Dso--R.N., Panye.T., Group. U.S.B of R. D. O. S. A., & Office, U. S. B. of R. D. S.(2000).Nonlinear Response of Steel Beams. U.S. Department of the interior. Bureau of Reclamation. Dam Safety Office.
11. Eurocode 4. EN 1994-1-2:2005: European Committee for Standardization, Brussels, 2005.
12. H. Yassin, F. Iqbal, A. Bagchi, and V.K.R. Kodur, (2017), Assessment of post-earthquake fire performance of steel-frame buildings, WCEE-14

13. Hong S, Varma AH. Analytical modeling of the standard fire behavior of loaded CFT columns. *Journal of Constructional Steel Research* 2009;65:54_69.
14. J. Myllymäki, T. T. Lie, and M. Chabot: NRC-CNRC Internal Report, No.673, Ottawa, Canada, 1994.
15. L. Twilt, R. Hass, W. Klingsch, M. Edwards, and D. Dutta: CIDECT design guide 4, Germany, 1995.
16. M. Chabot, and T. T. Lie: NRC-CNRC Internal Report, No.628, Ottawa, Canada, 1992.
17. Mohamed Dabaon, Saher El-Khoriby, Mahmoud El-Boghdadi, “Confinement effect of stiffened and unstiffened concrete-filled stainless steel tubular stub columns” Department of Structural Engineering, Tanta University, Tanta, Egypt
18. Reza Imani, Gilberto Mosqueda and Michel Bruneau (2014), Post-Earthquake Fire Resistance of Ductile Concrete-Filled Double-Skin Tube Columns, Technical Report-14-008
19. Romero ML, Moliner V, Espinos A, Ibanez C, Hospitaler A., Fire behavior of axially loaded slender high strength concrete-filled tubular columns, *Journal of Constructional Steel Research* 2011: 67(2);19
20. Scawthorn C., Eidinger J.M., and Schiff A.J., 2005. Fire following the earthquake. Technical Council on Lifeline Earthquake Engineering, Monograph No. 26, American Society of Civil Engineers (ASCE), Reston, VA
21. T. T. Lie, and M. Chabot: NRC-CNRC Internal Report, No.611, Ottawa, Canada, 1992.
22. Xiling LU and Weidong LU, Seismic behavior of concrete and steel composite columns under cyclic loading,12 WCEE
23. Y. Sakumoto, T. Okada, M. Yoshida, and S. Tasaka: *Journal of Materials in Civil Engineering*, Vol. 6 (1994), p. 169

Annexure

1. Horizontal load versus horizontal displacement hysteretic curves (Xilin Lu et al.)

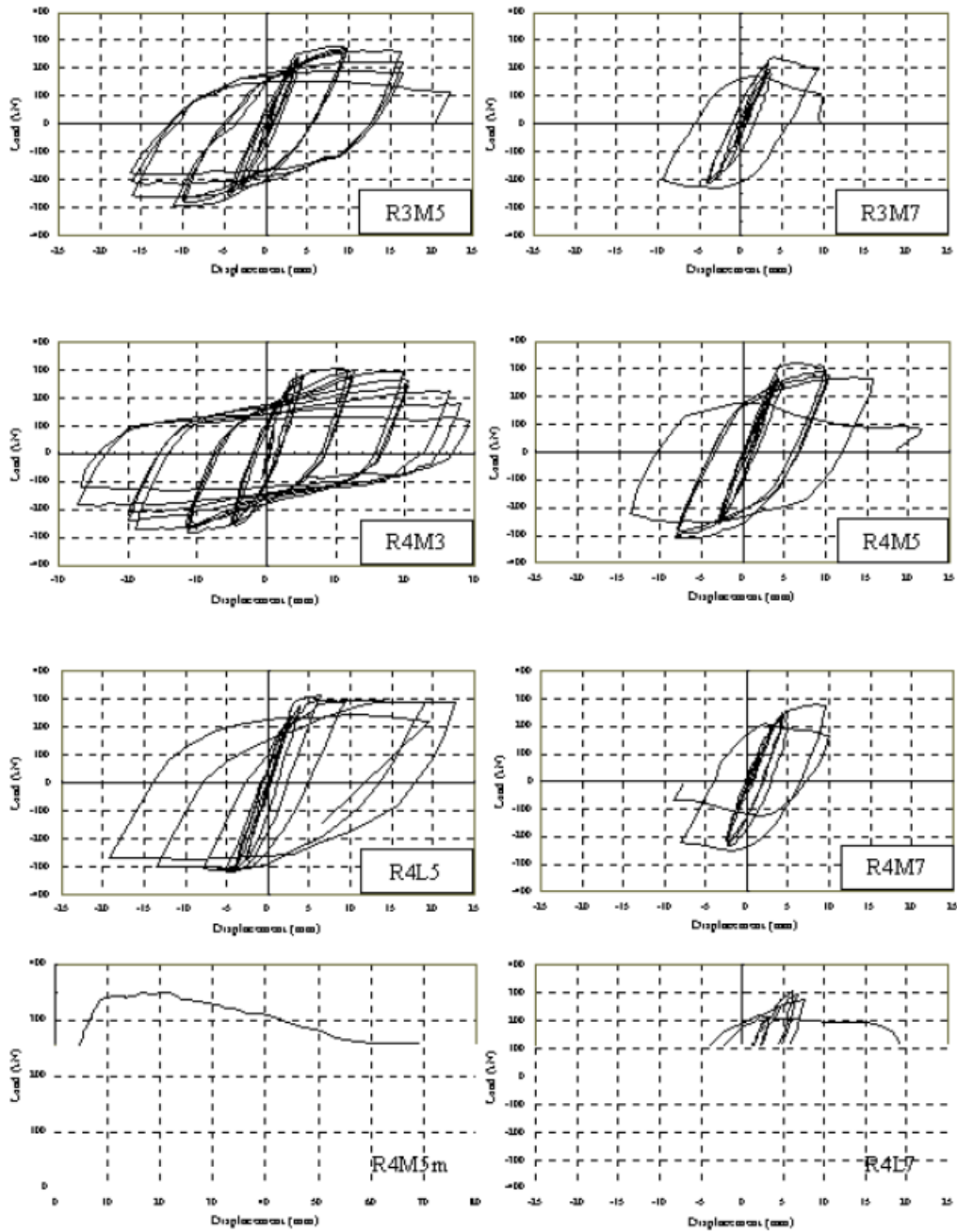


Fig.6 Horizontal load versus horizontal displacement hysteretic curves

2. Nonlinear isotropic/kinematic hardening model

The evolution law of this model consists of two components: a nonlinear kinematic hardening component, which describes the translation of the yield surface in stress space through the back stress, α ; and an isotropic hardening component, which describes the change of the equivalent stress defining the size of the yield surface, σ^0 , as a function of plastic deformation.

The kinematic hardening component is defined to be an additive combination of a purely kinematic term and a relaxation term (the *recall* term), which introduces the nonlinearity. When temperature and field variable dependencies are omitted, the hardening law is

$$\dot{\alpha} = C \frac{1}{\sigma^0} (\sigma - \alpha) \dot{\bar{\epsilon}}^{pl} - \gamma \alpha \dot{\bar{\epsilon}}^{pl}$$

where C and γ are material parameters that must be calibrated from cyclic test data. C is the initial kinematic hardening modulus, and γ determines the rate at which the kinematic hardening modulus decreases with increasing plastic deformation.

The isotropic hardening behavior of the model defines the evolution of the yield surface size, σ^0 , as a function of the equivalent plastic strain, $\bar{\epsilon}^{pl}$. This evolution can be introduced by specifying σ^0 directly as a function of $\bar{\epsilon}^{pl}$ in tabular form, by specifying σ^0 in

$$\sigma^0 = \sigma|_0 + Q_\infty (1 - e^{-b\bar{\epsilon}^{pl}})$$

where $\sigma|_0$ is the yield stress at zero plastic strain and Q_∞ and b are material parameters. Q_∞ is the maximum change in the size of the yield surface, and b defines the rate at which the size of the yield surface changes as plastic straining develops. When the equivalent stress defining the size of the yield surface remains constant ($\sigma^0 = \sigma|_0$), the model reduces to a nonlinear kinematic hardening model.

Kinematic hardening parameter:

C = kinematic hardening modulus.

γ = rate at which hardening modulus decreases with plastic straining (σ^0).

σ^0 = yield stress at zero plastic strain.

Isotropic hardening parameter:

Q = maximum change in the size of the yield surface.

b = rate at which σ^0 change with plastic strain

| C | γ | σ^0 | Q | b |
|------|----------|------------|--------|----|
| 3347 | 50 | 315 | 137.89 | 10 |

3. Material Properties

Thermal properties of Steel material at elevated temperatures

Formulation from Eurocode 2

Thermal elongation

The thermal strain $\epsilon_c(\theta)$ of concrete may be determined from the following with reference to the length at 20°C:

Siliceous aggregates:

$$\epsilon_c(\theta) = -1.8 \times 10^{-4} + 9 \times 10^{-6}\theta + 2.3 \times 10^{-11}\theta^3 \text{ for } 20^\circ\text{C} \leq \theta \leq 700^\circ\text{C}$$

$$\epsilon_c(\theta) = 14 \times 10^{-3} \text{ for } 700^\circ\text{C} < \theta \leq 1200^\circ\text{C}$$

Calcareous aggregates:

$$\epsilon_c(\theta) = -1.2 \times 10^{-4} + 6 \times 10^{-6}\theta + 1.4 \times 10^{-11}\theta^3 \text{ for } 20^\circ\text{C} \leq \theta \leq 805^\circ\text{C}$$

$$\epsilon_c(\theta) = 12 \times 10^{-3} \text{ for } 805^\circ\text{C} < \theta \leq 1200^\circ\text{C}$$

where θ is the concrete temperature (°C)

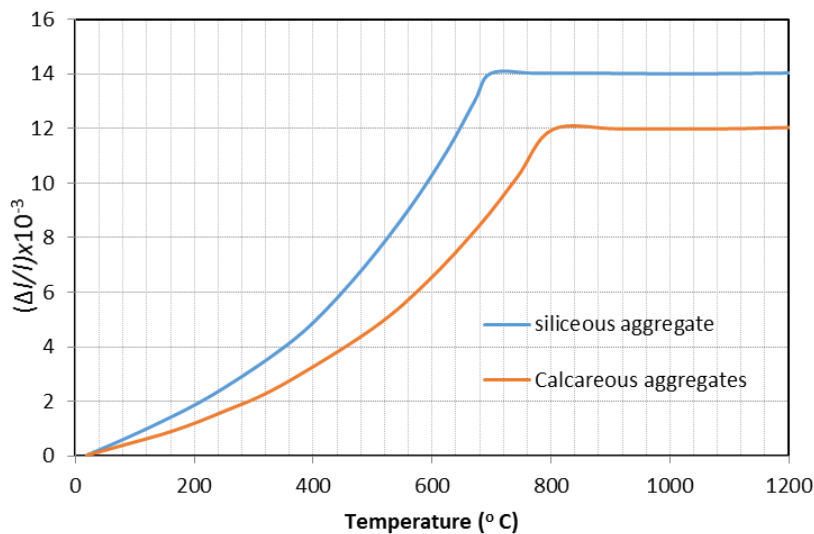


Figure 8: Thermal elongation of concrete at elevated temperature

Specific heat

The specific heat $c_p(\theta)$ of dry concrete ($u=0\%$) may be determined from the following:

Siliceous and calcareous aggregates:

$$c_p(\theta) = 900 \text{ (J/kg K)} \quad 20^\circ\text{C} \leq \theta \leq 100^\circ\text{C}$$

$$c_p(\theta) = 900 + (\theta - 100) \text{ (J/kg K)} \quad \text{for } 100^\circ\text{C} < \theta \leq 200^\circ\text{C}$$

$$c_p(\theta) = 1000 + (\theta - 200)/2 \text{ (J/kg K)} \quad \text{for } 200^\circ\text{C} < \theta \leq 400^\circ\text{C}$$

$$c_p(\theta) = 1100 \text{ (J/kg K)} \quad \text{for } 400^\circ\text{C} < \theta \leq 1200^\circ\text{C}$$

Thermal conductivity

Upper limit of thermal conductivity λ_c of normal weight concrete may be determined from:

$$\lambda_c = 2 - 0.2451 (\theta/100) + 0.0107 (\theta/100)^2 \text{ W/m K} \quad \text{for } 20^\circ\text{C} \leq \theta \leq 1200^\circ\text{C}$$

where θ is the concrete temperature

Lower limit of thermal conductivity λ_c of normal weight concrete may be determined from:

$$\lambda_c = 1.36 - 0.136 (\theta/100) + 0.0057 (\theta/100)^2 \text{ W/m K} \quad \text{for } 20^\circ\text{C} \leq \theta \leq 1200^\circ\text{C}$$

EC4 recommends the use of an upper limit of steel concrete composite members.

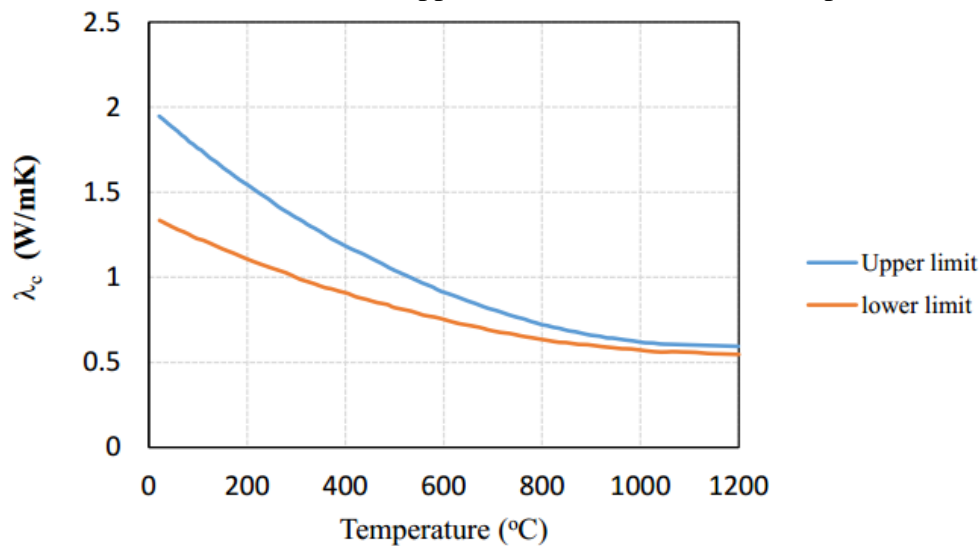


Figure 9: Thermal conductivity of concrete at elevated temperature

Formulation from lie

Lie (1984) have proposed different formulations for the thermal properties of concrete at elevated temperatures.

Thermal capacity

The thermal capacity of concrete may be determined by means of following expressions:

$$\rho_c c_c = 2.566 \times 10^6 \text{ J/(m}^3\text{°C)} \quad \text{for } 0 \leq \theta \leq 400^\circ\text{C}$$

$$\rho_c c_c = (0.1765 \theta - 68.034) \times 10^6 \text{ J/(m}^3\text{°C)} \quad \text{for } 400 < \theta \leq 410^\circ\text{C}$$

$$\rho_c c_c = (-0.05043 \theta - 25.00671) \times 10^6 \text{ J/(m}^3\text{°C)} \quad \text{for } 410 < \theta \leq 445^\circ\text{C}$$

$$\rho_c c_c = 2.566 \times 10^6 \text{ J/(m}^3\text{°C)} \quad \text{for } 445 < \theta \leq 500^\circ\text{C}$$

$$\rho_c c_c = (0.01603 \theta - 5.44881) \times 10^6 \text{ J/(m}^3\text{°C)} \quad \text{for } 500 < \theta \leq 635^\circ\text{C}$$

$$\rho_c c_c = (0.16635 \theta - 100.90225) \times 10^6 \text{ J/(m}^3\text{°C)} \quad \text{for } 635 < \theta \leq 715^\circ\text{C}$$

$$\rho_c c_c = (-0.22103 \theta - 176.07343) \times 10^6 \text{ J/(m}^3\text{°C)} \quad \text{for } 715 < \theta \leq 785^\circ\text{C}$$

$$\rho_c c_c = 2.566 \times 10^6 \text{ J/(m}^3\text{°C)} \quad \text{for } \theta > 785^\circ\text{C}$$

where θ is the concrete temperature

Thermal conductivity

$$\lambda_c = 1.355 \text{ W/(m}^\circ\text{C)} \quad \text{for } 0 \leq \theta \leq 293^\circ\text{C}$$

$$\lambda_c = -0.001241 \lambda_c + 1.7162 \text{ W/(m}^\circ\text{C)} \text{ for } \theta > 293^\circ\text{C}$$

Thermal expansion coefficient

$$\alpha_c = (0.008 \theta + 6) \times 10^{-6} \text{ m/(m}^\circ\text{C)}$$

where θ is the concrete temperature

Thermal properties of Steel material at elevated temperatures

Formulation from Eurocode 2

Thermal elongation

The thermal elongation of steel $\Delta l/l$ should be determined from the following:

$$\Delta l/l = 1.2 \times 10^{-5} \theta + 0.4 \times 10^{-8} \theta^2 - 2.416 \times 10^{-4} \quad \text{for } 20^\circ\text{C} \leq \theta < 750^\circ\text{C}$$

$$\Delta l/l = 1.1 \times 10^{-2} \theta \quad \text{for } 750^\circ\text{C} \leq \theta \leq 860^\circ\text{C}$$

$$\Delta l/l = 2 \times 10^{-5} \theta - 6.2 \times 10^{-3} \quad \text{for } 860^\circ\text{C} < \theta \leq 1200^\circ\text{C}$$

where: l is the length at 20°C
 Δl is the temperature induced elongation
 θ is the steel temperature [$^\circ\text{C}$]

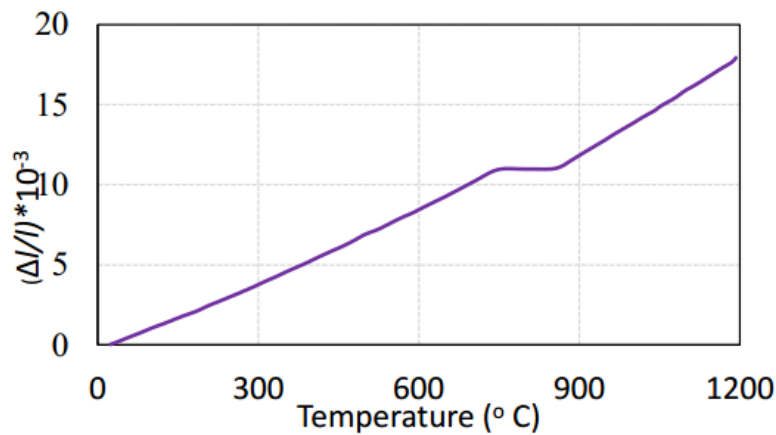


Figure 10: Thermal elongation of steel with temperature

Specific heat

The specific heat $c_a(\theta)$ of steel may be determined from the following:

$$c_a = 425 + 7.73 \times 10^{-1} \theta - 1.69 \times 10^{-3} \theta^2 + 2.22 \times 10^{-6} \theta^3 \text{ J/kgK} \quad \text{for } 20^\circ\text{C} \leq \theta < 600^\circ\text{C}$$

$$c_a = 666 + \frac{13002}{738 - \theta} \text{ J/kgK} \quad \text{for } 600^\circ\text{C} \leq \theta < 735^\circ\text{C}$$

$$c_a = 545 + \frac{17820}{\theta - 731} \text{ J/kgK} \quad \text{for } 735^\circ\text{C} \leq \theta < 900^\circ\text{C}$$

$$c_a = 650 \text{ J/kgK} \quad \text{for } 900^\circ\text{C} \leq \theta \leq 1200^\circ\text{C}$$

where θ is the steel temperature

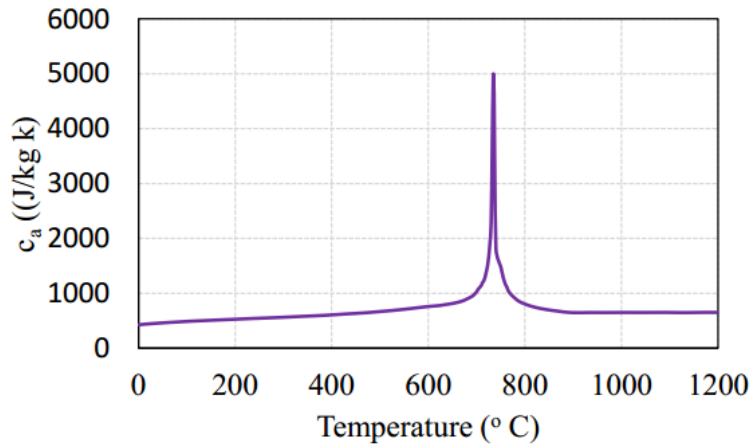


Figure 11: Specific heat of steel with temperature

Thermal conductivity

The thermal conductivity of steel λ should be determined from the following

$$\lambda = 54 - 3.33 \times 10^{-2} \theta \text{ W/mK} \quad \text{for } 20^\circ\text{C} \leq \theta < 800^\circ\text{C}$$

$$\lambda = 27.3 \text{ W/mK} \quad \text{for } 800^\circ\text{C} \leq \theta \leq 1200^\circ\text{C}$$

where θ is the steel temperature

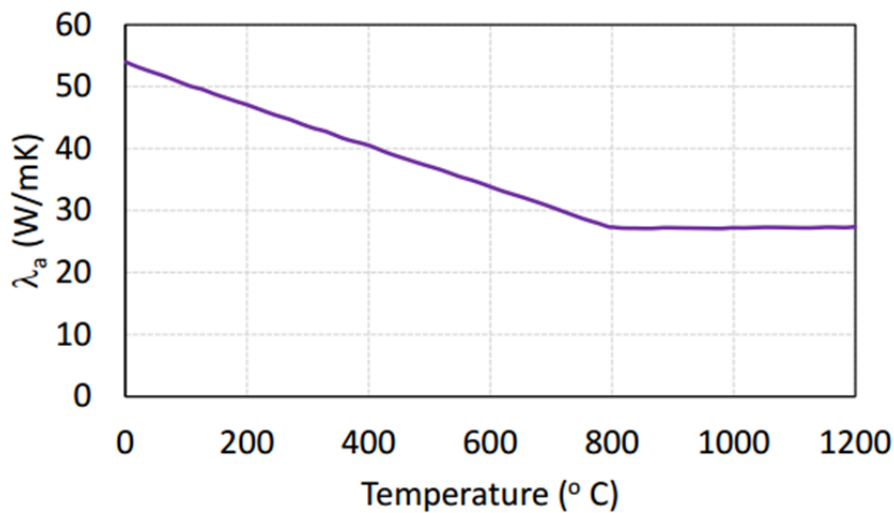


Figure 12: Thermal conductivity of steel with temperature

Formulation from Lie

Lie (1984) proposed different equations for the thermal properties of steel at elevated temperatures

Thermal capacity

$$\rho_a c_a = (0.004 \times \theta - 3.3) \times 10^6 \text{ (J/m}^3\text{°C)} \quad \text{for } 0^\circ\text{C} < \theta \leq 650^\circ\text{C}$$

$$\rho_a c_a = (0.0068 \times \theta - 38.3) \times 10^6 \text{ (J/m}^3\text{°C)} \quad \text{for } 650^\circ\text{C} < \theta \leq 725^\circ\text{C}$$

$$\rho_a c_a = (-0.086 \times \theta + 73.35) \times 10^6 \text{ (J/m}^3\text{°C)} \quad \text{for } 725^\circ\text{C} < \theta \leq 800^\circ\text{C}$$

$$\rho_a c_a = 4.55 \times 10^6 \text{ (J/m}^3\text{°C)} \quad \text{for } \theta \geq 800^\circ\text{C}$$

Thermal conductivity

The thermal conductivity of steel λ_a is given by:

$$\lambda_a = -0.022 \times \theta + 48 \text{ (W/m}^\circ\text{C)} \quad \text{for } 0^\circ\text{C} < \theta \leq 900^\circ\text{C}$$

$$\lambda_a = 28.2 \text{ (W/m}^\circ\text{C)} \quad \text{for } \theta > 900^\circ\text{C}$$

Thermal expansion coefficient (α_a)

$$\alpha_a = (0.004 \theta + 12) \times 10^{-6} \text{ (m/m}^\circ\text{C)} \quad \text{for } 0^\circ\text{C} < \theta \leq 1000^\circ\text{C}$$

$$\alpha_a = 16 \times 10^{-6} \text{ (m/m}^\circ\text{C)} \quad \text{for } \theta \geq 1000^\circ\text{C}$$

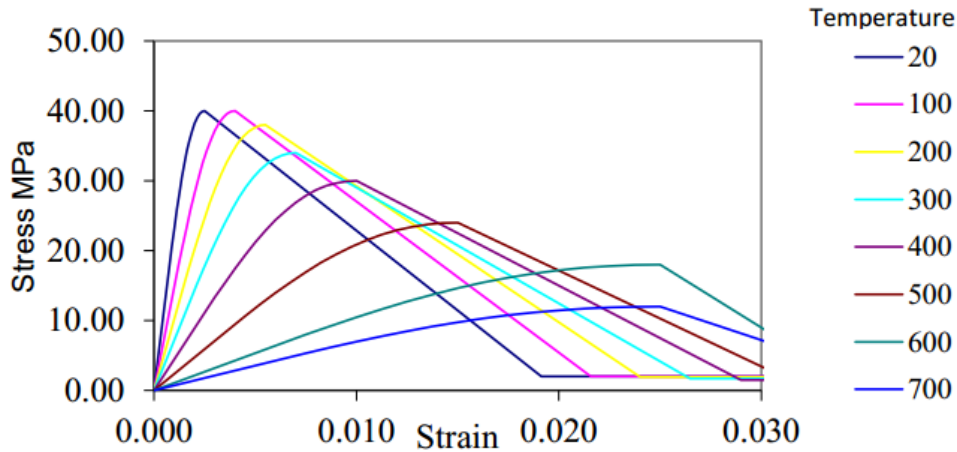


Figure 13: Stress strain curve for concrete at elevated temperatures (Eurocode)

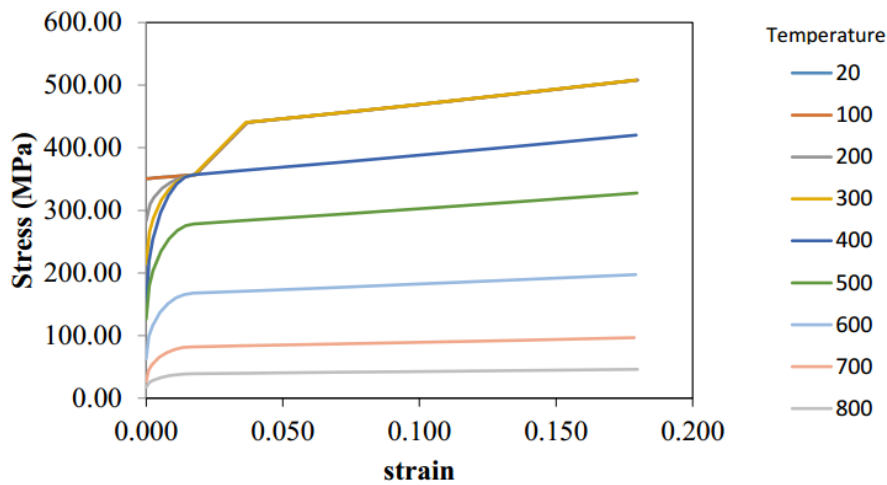


Figure 14: Stress strain curve for steel at elevated temperatures (Eurocode)

Calculation method for composite columns in Clause 4.3.5.1 of EN 1994-1-2

In this method, the design value of the resistance of composite columns in axial compression exposed to fire ($N_{fi,Rd}$) is calculated as:

$$N_{fi,Rd} = \chi N_{fi,pl,Rd}$$

where

χ is the reduction coefficient for buckling curve ‘c’ given in Clause 6.3.1.2 of EN 1993-1-1 obtained from the value of the relative slenderness at elevated temperature

$N_{fi,pl,Rd}$ is the design value of the plastic resistance to axial compression in the fire situation

The design value of the plastic resistance of the cross-section in the fire situation ($N_{fi,pl,Rd}$) is given by:

$$N_{fi,pl,Rd} = \sum_j (A_{a,\theta} f_{ay,\theta}) / \gamma_{M,fi,a} + \sum_k (A_{s,\theta} f_{sy,\theta}) / \gamma_{M,fi,s} + \sum_m (A_{c,\theta} f_{c,\theta}) / \gamma_{M,fi,c}$$

where:

$A_{i,\theta}$ is the area of each element of the cross-section ($i = a$ or c or s), which may be affected by the fire

The effective flexural stiffness of the column can be calculated through:

$$(EI)_{fi,eff} = \sum_j (\Phi_{a,\theta} E_{a,\theta} I_{a,\theta}) + \sum_k (\Phi_{s,\theta} E_{s,\theta} I_{s,\theta}) + \sum_m (\Phi_{c,\theta} E_{c,sec,\theta} I_{c,\theta})$$

where:

$I_{i,\theta}$ is the second moment of area, of the partially reduced part i of the cross-section for bending around the weak or strong axis,

$\Phi_{a,\theta}$ is the reduction coefficient depending on the effect of thermal stresses.

$E_{c,sec,\theta}$ is the characteristic value for the secant modulus of concrete in the fire situation

For concrete filled sections, the values of reduction coefficients are not yet established so they are taken as unity.

The Euler buckling load or elastic critical load in the fire situation is as follows:

$$N_{fi,cr} = \pi^2 (EI)_{fi,eff} / l_{\theta}^2$$

where:

l_{θ} is the buckling length of the column in the fire situation

The relative slenderness of the column at elevated temperatures is given by:

$$\lambda_{\theta} = \sqrt{(N_{fi,pl,R} / N_{fi,cr})}$$

where $N_{fi,pl,R}$ is the value of $N_{fi,pl,Rd}$ when the material factors are taken as 1.0. This value of relative slenderness is used to enter to the buckling curve ‘c’, from where the reduction coefficient χ needed for determining the buckling load is obtained.